

LOCAL MOLECULAR GAS TOWARD THE AQUILA RIFT REGION

YANG SU,¹ JI YANG,^{1,2} QING-ZENG YAN,¹ YAN GONG,^{1,3} ZHIWEI CHEN,¹
SHAOBO ZHANG,¹ YAN SUN,¹ MIAOMIAO ZHANG,¹ XUEPENG CHEN,^{1,2} XIN ZHOU,¹
MIN WANG,¹ HONGCHI WANG,^{1,2} YE XU,¹ AND ZHIBO JIANG¹

¹*Purple Mountain Observatory and Key Laboratory of Radio Astronomy, Chinese Academy of Sciences, Nanjing 210023, China*

²*School of Astronomy and Space Science, University of Science and Technology of China, 96 Jinzhai Road, Hefei 230026, China*

³*Max-Planck Institute für Radioastronomie, Auf dem Hügel 69, D-53121 Bonn, Germany*

ABSTRACT

We present the results of a ~ 250 square degrees CO mapping ($+26^\circ \lesssim l \lesssim +50^\circ$ and $-5^\circ \lesssim b \lesssim +5^\circ$) toward the Aquila Rift region at a spatial resolution of $\sim 50''$ and a grid spacing of $30''$. The high dynamic range CO maps with a spectral resolution of $\sim 0.2 \text{ km s}^{-1}$ display highly structured molecular cloud (MC) morphologies with valuable velocity information, revealing complex spatial and dynamical features of the local molecular gas. In combination with the MWISP CO data and the Gaia DR2, distances of the main MC structures in the local ISM are well determined toward the Aquila Rift region. We find that the total MC mass within 1 kpc is about $\gtrsim 4.1 \times 10^5 M_\odot$ in the whole region. In fact, the mass of the molecular gas is dominated by the W40 giant molecular cloud (GMC) at ~ 474 pc ($\sim 1.4 \times 10^5 M_\odot$) and the GMC complex G036.0+01.0 at ~ 560 – 670 pc ($\sim 2.0 \times 10^5 M_\odot$), while the MCs at ~ 220 – 260 pc have gas masses of $\sim 10^2$ – $10^3 M_\odot$. Interestingly, an ~ 80 pc long filamentary MC G044.0–02.5 at a distance of ~ 404 pc shows a systematic velocity gradient along and perpendicular to the major axis of the filament. The HI gas with the enhanced emission has the similar spatial morphologies and velocity features compared to the corresponding CO structure, indicating that the large-scale converging HI flows are probably responsible for the formation of the MC. Meanwhile, the long filamentary MC consists of many sub-filaments with the lengths ranging from ~ 0.5 pc to several pc, as well as prevalent networks of filaments in other large-scale local MCs.

Keywords: ISM: clouds – ISM: molecules – ISM: kinematics and dynamics – radio lines: ISM – stars: formation – surveys

Corresponding author: Yang Su
yangsu@pmo.ac.cn

1. INTRODUCTION

A substantial amount of interstellar gas in the Milky Way is in molecular clouds (MCs) and star formation is believed to occur in dense regions of MCs. MCs are therefore important in studying the nature of the cold and dense molecular gas in the interstellar medium (ISM). Detailed studies can provide us with the solid knowledge of the properties of MCs, such as the morphology, distribution, and dynamics of the molecular gas. In observations, MCs are generally traced by CO emission because of its low excitation energy, low critical density, and easy detection over other gas tracers (Bolatto et al. 2013; Heyer & Dame 2015). Actually, a lot of CO surveys have been done to study the molecular gas in the Galaxy (e.g., Heyer et al. 1998; Dame et al. 2001; Burton et al. 2013; Barnes et al. 2015; Heyer & Dame 2015).

Among the most important surveys is the Milky Way Imaging Scroll Painting (MWISP¹) project, which provides the unbiased ^{12}CO , ^{13}CO , and C^{18}O ($J=1-0$) database toward the northern Galactic plane for regions of $l = -10^\circ$ to $+250^\circ$ and $|b| \lesssim 5.2$. The survey data sets of the MWISP have a large spatial dynamic range, high sensitivity, and high-velocity resolution for CO and its isotopes (see Table 1 and Section 2.3 in Su et al. 2019). Due to these characteristics and advantages, the MWISP CO data provided us with a good opportunity to unveil the nature of the MCs as well as the structures of the Milky Way in our previous studies (i.e., Su et al. 2016; Sun et al. 2017). These large-scale CO maps with the high sensitivity on a fully sampled angular grid of $30''$ also allow us to investigate details of MCs' structures and dynamics, especially for local MCs due to their small distances.

One can use the optically thick ^{12}CO emission to trace the enveloping layer (i.e., $\sim 10^2 \text{ cm}^{-3}$) of extended MCs and to reveal the dynamical features of the molecular gas of low surface brightness. On the other hand, the optically thin ^{13}CO and C^{18}O emission can trace the denser region (i.e., $\sim 10^3 - 10^4 \text{ cm}^{-3}$) in local MCs. In particular, the enhanced concentration of C^{18}O emission seems to be associated with star-forming regions. Using the abundant data of ^{12}CO , ^{13}CO , and C^{18}O , we can obtain valuable information on the physical properties of the local MCs and star formation activities in MCs.

So far, an excellent case is the 100 deg^2 CO mapping toward the nearby Taurus MC, in which the researchers reveal a very complex and highly structured molecular-gas morphology using the FCRAO 13.7 m telescope (Goldsmith et al. 2008; Narayanan et al. 2008). Thanks to the high sensitivities of the MWISP, the large-scale CO survey can be extended to other nearby MCs, which will shed light on detailed structures, distributions, and dynamics of the local molecular gas.

In this paper, we focus on the local MCs toward the Aquila Rift region near the Galactic plane, i.e., the region in the first quadrant of $l = +25.8$ to $+49.7$ and $|b| \lesssim 5.2$. This region has been fully covered by observations of the MWISP over

¹ <http://english.dlh.pmo.cas.cn/ic/>

the past seven years. In section 2, we briefly describe the observations and data. Section 3 shows the results and some discussions of the local molecular gas by taking advantages of the high spatial dynamic range CO images. Based on the properties of the local MCs, such as distances, mass distributions, and velocity structures of the gas, we construct panoramic views of the local MCs ($\lesssim 1$ kpc) by combining the MWISP CO data and the Gaia DR2 data. Finally, we summarize the new findings and main conclusions in Section 4.

2. OBSERVATIONS AND DATA

The observations and data are part of the MWISP project that is described in our previous paper (Su et al. 2019). Briefly, the ~ 250 deg² region of $l = +25^\circ.8$ to $+49^\circ.7$ and $|b| \lesssim 5^\circ.2$ was covered between 2011 November and 2018 April with the 3×3 multibeam sideband-separating Superconducting Spectroscopic Array Receiver (SSAR) system (Shan et al. 2012) on the Delingha 13.7 m telescope. The ^{12}CO , ^{13}CO , and C^{18}O ($J=1-0$) lines were simultaneously observed using the position-switch On-The-Fly (OTF; see Sun et al. 2018) mode. The half-power beam width (HPBW) is $\sim 50''$ at a frequency of ~ 110 – 115 GHz. The tracking accuracy and the pointing accuracy are $\sim 1''$ – $3''$ and $\lesssim 5''$, respectively.

The whole region was divided into 1001 cells of $30' \times 30'$, each being mapped along the Galactic longitude (l) and latitude (b) at least twice. After fitting the first-order (or linear) baseline, the final three-dimensional (3D) FITS data have typical rms noise levels of ~ 0.5 K for ^{12}CO ($J=1-0$) at a channel width of 0.16 km s^{-1} and ~ 0.3 K for ^{13}CO ($J=1-0$) and C^{18}O ($J=1-0$) at 0.17 km s^{-1} with a uniform grid spacing of $30''$. Here, the main beam temperature is calibrated based on $T_{\text{MB}} = T_{\text{A}}^* / (f_{\text{b}} \times \eta_{\text{MB}})$, and the filling factor f_{b} was assumed to be 1 for the CO emission. The data were reduced using the GILDAS software².

3. RESULTS AND DISCUSSIONS

3.1. Overall Distribution of the Local CO Gas

Here, we study the properties of the local MCs using the MWISP ^{12}CO , ^{13}CO , and C^{18}O data. In the previous study, we have shown that the local MCs toward the region of $l = +25^\circ.8$ to $+49^\circ.7$ and $|b| \lesssim 5^\circ.2$ are mainly in the velocity range of 0 – 20 km s^{-1} (see Figures 6, 7, and 9 in Su et al. 2019). In this region, the prominent feature is the ~ 200 square degrees dark lane seen in the optical image, which is called the Aquila Rift (e.g., see the review in Prato et al. 2008). A considerable amount of molecular gas is situated in the Aquila Rift, which was investigated by some authors based on the previous 1.2 m telescope survey (Dame & Thaddeus 1985; Dame et al. 1987) and the recent 1.85 m telescope survey (Nakamura et al. 2017). The whole Aquila Rift is a large extended region (i.e., $l \sim +20^\circ$ to $+50^\circ$ and $b \sim -5^\circ$ to $+10^\circ$) and is not fully covered by the MWISP survey ($|b| \lesssim 5^\circ.2$). However, the MWSIP

² <http://ascl.net/1305.010> or <http://www.iram.fr/IRAMFR/GILDAS>

data have the higher angular resolution and sensitivity (Su et al. 2019), which allow us to search for new observational features and to study the properties of the local molecular gas.

Figure 1 displays the ^{12}CO ($J=1-0$, blue), ^{13}CO ($J=1-0$, green), and C^{18}O ($J=1-0$, red) intensity map in the $[-1, 25] \text{ km s}^{-1}$. Note that in this velocity interval, CO emission of the local gas near regions of $b \sim 0^\circ$ suffers some contamination from the Perseus arm (e.g., see Table 1 in Reid et al. 2019). However, this effect is not serious because of the limited extension of the Perseus gas at larger distances. Obviously, the molecular gas traced by the large-scale extended CO emission displays complex structures and plentiful details in the mapped region. Many CO structures, such as filaments, arcs/shells/bubbles, finger-like protrusions, and other irregular morphologies, are unveiled due to the high dynamic range of our survey.

Some MCs with relatively strong ^{13}CO and/or C^{18}O emission are found to be embedded in the enveloping structures traced by the faint, diffuse, and extended ^{12}CO emission. The multiple layers traced by the ^{12}CO , ^{13}CO , and C^{18}O emission, together with different velocity components and, therefore, probably different distances (see Section 3.2), help us construct a useful panoramic 3D picture of the local molecular gas.

Figure 2 displays the peak temperature of the ^{12}CO emission, the peak temperature of the ^{13}CO emission, and the velocity distribution of the ^{13}CO emission for the local molecular gas in the covered region. For a total of $\sim 3.5 \times 10^6$ pixels on a $30''$ grid, about a half of the samples in the coverage have detected ^{12}CO emission, while only $\sim 20\%$ ($\sim 0.7\%$) pixels have ^{13}CO (C^{18}O) emission (Figure 3). For the detectable ^{12}CO emission, over 50% of ^{12}CO samples have a peak temperature less than 4 K, indicating subthermal excitation of CO emission for the low-density molecular gas in the local ISM.

The ^{12}CO gas with higher peak temperature (i.e., $T_{\text{peak}12} \gtrsim 10 \text{ K}$) is roughly associated with the nearby star formation activities, i.e., the H II region W40 at ($l = 28^\circ 75'$, $b = 3^\circ 51'$), the Serpens NE Cluster at ($l = 31^\circ 74'$, $b = 3^\circ 12'$) (Herczeg et al. 2019), and the LBN 031.75+04.98 (see red circles in Figure 2). This result is consistent with the work of Wang et al. (2019) for the Gemini OB1 MCs, where the authors show that the high-temperature CO gas is related to nearby massive star-forming regions. The two red rectangles near the Galactic plane show other regions with high ^{12}CO temperature but lacking distance information. We speculate that the surrounding star formation activities are probably responsible for the higher CO temperatures there.

The optical depths of the ^{13}CO and C^{18}O lines can be estimated using equations described in Su et al. (2015). In brief, we assume that the excitation temperatures (T_{ex}) of the ^{13}CO and C^{18}O lines have the same value as that of the optically thick ^{12}CO line, and the beam filling factor of the gas, f_b , is assumed to be 1. Note that the estimated optical depth of τ_{13} (τ_{18}) is related to the values of T_{ex} , f_b , and $T_{\text{mb}13}$ ($T_{\text{mb}18}$). Therefore, the estimated τ_{13} is likely to be a lower limit because of the

possible underestimated $T_{\text{mb}13}$ (i.e., self absorption of ^{13}CO emission). On the other hand, τ_{18} is likely overestimated due to the underestimated T_{ex} from ^{12}CO emission (i.e., self absorption of ^{12}CO emission).

For the entire coverage, about 82% of detected ^{13}CO gas shows a low optical depth, $\lesssim 0.6$, indicating the dominant optically thin ^{13}CO emission in the local MCs. However, the optical depth of the ^{13}CO line is not always below one. A few ^{13}CO points ($\lesssim 4\%$) have $\tau_{13} \gtrsim 1$, especially in regions near the H II region W40. The high-density gas traced by the strong C^{18}O emission is also mainly located near such regions (e.g., see red contours in Figure 2, also see Section 3.3.2 in [Su et al. 2019](#)). In fact, τ_{18} is always < 1 , confirming that C^{18}O emission is optically thin in the Aquila Rift region.

Compared to the optically thick ^{12}CO emission, the distribution of the optically thin ^{13}CO and C^{18}O emission is obviously diminished and is limited in the interior of the envelope traced by the extended ^{12}CO emission (Figures 1 and 2). Despite this, the ^{13}CO emission successfully traces the main body of the local MCs because of the high dynamic range and sensitive observations. The velocity field of the dense molecular gas is also well described by the first moment of the ^{13}CO emission. Moreover, the concentration of the C^{18}O gas represents the local dense gas region, where star formation activities are ongoing (i.e., many HH objects in LDN 673 discovered by [Rector et al. 2018](#); thousands of young stars and protostars in Serpens MC, W40 region, and Sh 2-62 studied by [Herczeg et al. 2019](#)).

On the other hand, there are some C^{18}O regions with relatively low ^{12}CO temperatures (e.g., the blue rectangle region for the $13\text{--}15\text{ km s}^{-1}$ gas in Figure 2). The information of star formation near these regions is unclear. We speculate that these regions are probably in the early evolutionary stage of star formation (e.g., see the case of the Serpens filament investigated by [Gong et al. 2018](#)). The Serpens filament is believed to be accreting material in the very early evolutionary stage of star formation, leading to a lower ^{12}CO temperature (self absorption) and strong C^{18}O emission. In fact, ^{13}CO emission in some positions also displays a self-absorption feature compared to the optically thin C^{18}O emission. We will study these samples in the future based on multi-wavelength data and statistical methods (e.g., see studies in [Wang et al. 2019](#)).

Figure 4 describes the molecular-gas distribution via the traditional position–velocity (PV) diagrams along $b = +4^\circ, +2^\circ, -2^\circ$, and -4° , respectively. Roughly, the CO emission in the observed area can be divided into three main parts: the molecular gas at (1) $l \sim +26^\circ$ to $+33^\circ$ with $V_{\text{LSR}} \sim 0\text{--}15\text{ km s}^{-1}$, (2) $l \sim +32^\circ$ to $+41^\circ$ with $V_{\text{LSR}} \sim 10\text{--}20\text{ km s}^{-1}$, and (3) $l \sim +40^\circ$ to $+50^\circ$ with $V_{\text{LSR}} \sim 3\text{--}11\text{ km s}^{-1}$. Again, the main body of local MCs is well described by the ^{13}CO emission (contours in the figure), which is similar to results shown in Figure 1. For comparison, the peak-temperature and velocity distributions of ^{13}CO emission in Figure 2 also show similar results: MCs are mainly concentrated in well-defined space and velocity ranges. We investigate the properties of the molecular gas via

these defined sub-regions, as well as the coherent spatial and velocity structures of the local MCs in Section 3.4.

3.2. Distances of the Local MCs

MCs with similar LSR velocities can be located at quite different distances. The situation is even more serious for the complex MCs with multi-velocity components in the first quadrant. Therefore, a more accurate distance is very important in studying the physical properties of the local MCs. In this work, distances of local MCs are estimated based on the Gaia DR2 data (Gaia Collaboration et al. 2016, 2018). The method is simple and straightforward since the extinction is determined by the amount of dust along the line of sight (LOS). Assuming that the extinction of a local MC is mainly determined by the dust in the cloud, the extinction (A_G) of stars behind the MC will be obviously larger than that of stars in front of the MC. The key point is how to pick up the jump correctly in the parallax- A_G space. Here, we employ the Markov Chain Monte Carlo (MCMC) algorithm discussed very recently by Yan et al. (2019).

To obtain a more accurate distance estimation of the local molecular gas, we must define the structure of the MCs first. Generally, the CO data are viewed channel by channel to search for coherent MC structures in the velocity field on a scale of several degrees. The selected MC structures with coherent velocity features are also checked in the corresponding PV diagrams. The boundary of an MC is then defined by the selected velocity interval with the selected threshold of the integrated CO intensity, which is crucial for the subsequent analysis.

Briefly, there are two cases in the definition of the CO structure. One case is the overlapping MCs with adjacent LSR velocities. The non-overlapping velocity intervals are integrated to show the distribution of the different MCs. That is, for individual examples, the overlapping MCs are divided into different parts based on their LSR velocities (e.g., MCs G030.5–01.5 and MCs G029.0–2.0a in Figure 5) or spatial distributions (e.g., GMC G036.0+01.0 in Figure 7). And then the individual CO structures can be used to calculate the corresponding distance of the MCs. The overlapping parts of MCs in an area are usually avoided in the estimation of the distance (e.g., see W40a and W40b in Figure 5). Regions near the Galactic plane are also avoided due to the complex gas environments there. The other case is the MCs with little velocity confusion. We used all CO emission in the velocity interval to define the MC structure, e.g., MC G044.0–02.5. The distance of the MC is estimated by using the whole CO structure. We also divided the single MC into several sub-regions to check the consistency of the distance estimation (see Figure 8).

The integrated-intensity threshold of a defined MC is roughly $\gtrsim 3\text{--}5 \text{ K km s}^{-1}$, depending on the cloud properties (i.e., sizes, environments, and locations). The threshold of the CO intensity is different for different MC structures. For example, the thresholds of MCs are $\sim 3\text{--}5 \text{ K km s}^{-1}$ for the W40a region and $\sim 10\text{--}15 \text{ K km s}^{-1}$

for the W40b region, respectively. Based on the CO structure from the selected velocity interval, the A_G of stars within the MC are then sorted according to the distances of stars. Using the MCMC algorithm, the jump point of on-cloud A_G in the distance- A_G space is picked up to estimate the distance of the CO cloud. We also check the validity of the distance estimation by comparing the A_G distribution of the nearby off-cloud samples with that of on-cloud samples. Results with large uncertainties are excluded according to the comparison between the on-cloud A_G and off-cloud A_G .

Generally, the estimated distance error of local MCs is less than 5%, which is mainly from the uncertainties in A_G , the different properties of the MCs (i.e., size, structure/morphology, and column density, etc.), and the contamination of other gas components along the LOS. As a result, the distance error is relatively small for large-scale MCs with the strong CO emission (i.e., MC structure with a sky coverage of several square degrees and CO integrated intensity of $\gtrsim 10 \text{ K km s}^{-1}$). On the other hand, the dust in some extended foreground cloud leads to the complicated distribution of A_G along the LOS. It is thus hard to calculate the distance of individual MCs in the region with multi-velocity components, e.g., MCs near the Galactic plane. In some cases, the distance of small CO patches cannot be determined due to the limited on-cloud Gaia samples. Despite this, some small MCs with coherent velocity and spatial structures can be considered together to estimate the distance of the molecular gas on a large scale (see rectangles in Figure 6). Meanwhile, distances of some CO structures with weak emission (i.e., $\lesssim 3\text{--}5 \text{ K km s}^{-1}$) cannot be obtained because of the low column density of MCs and the large A_G error of stars.

With the method discussed above, distances of some large-scale CO structures are successfully determined for the local MCs based on the MWISP CO data and the Gaia DR2 (see Table 1). All selected regions with estimated distance are labeled in Figures 5–8. These MCs are distributed in a large distance range of $\sim 220\text{--}770 \text{ pc}$ in the whole region. In the region of $l \sim +26^\circ$ to $+33^\circ$ (Figure 5), the dominant CO gas, which is mainly associated with the Serpens clusters and the H II W40 region, is located at $\sim 470 \text{ pc}$. Our results roughly agree with the previous studies based on VLBA measurements (i.e., $436.0 \pm 9.2 \text{ pc}$ in Ortiz-León et al. 2017) and the independent analysis from Gaia DR2 (i.e., $\sim 400\text{--}500 \text{ pc}$ in Ortiz-León et al. 2018; Zucker et al. 2019). In regions of $b \lesssim 0^\circ$, some interesting MC structures are located at $\sim 400\text{--}550 \text{ pc}$. Interestingly, toward the region of $l \sim +26^\circ$ to $+33^\circ$, considerable molecular gas at $\sim 240\text{--}260 \text{ pc}$ is situated in front of the $\sim 400\text{--}550 \text{ pc}$ MCs (see the left panel of Figure 5), which leads to some controversy over MC distances in previous studies (e.g., see discussions and references in Nakamura et al. 2017). Additionally, the nearer MCs at $\sim 220\text{--}240 \text{ pc}$ also extend from the $l \sim +36^\circ$ to $+44^\circ$ region with larger LSR velocities (Figure 6).

Toward the region of $l \sim +32^\circ$ to $+41^\circ$, the distribution of the local molecular gas is quite complicated. Many small MCs are estimated to be at $\sim 220\text{--}240 \text{ pc}$ (Figure 6),

and some CO clouds are located at ~ 610 pc; although, these MCs cannot be easily identified due to their complex and intricate velocity components. Nevertheless, we suggest that most of the molecular gas in the region is located at a distance range of ~ 560 – 670 pc based on Figures 6 and 7. By considering the mass, the extended size, and the distance error (i.e., $\lesssim 5\%$, 20 – 30 pc) of the molecular gas, we defined a GMC named as G036.0+01.0 (the nickname of “Phoenix cloud”). This GMC is located at about ~ 610 pc and is less studied in the previous literature.

Toward $l \sim +40^\circ$ to $+50^\circ$, the molecular gas is dominated in the $b \lesssim 0^\circ$ region. Two local MCs with little contamination from other velocity components are estimated to be located at ~ 400 pc and ~ 770 pc, respectively. We identified the prominent ~ 404 pc MC feature as MC G044.0–02.5 (the nickname of “River cloud”; Figure 8), which was named as Cloud B in previous studies (e.g., see Dame & Thaddeus 1985; Dame et al. 1987). We also note that the Cloud A at ~ 25 – 27 km s $^{-1}$ (Dame & Thaddeus 1985; Dame et al. 1987) probably has a distance of $\gtrsim 1.1$ kpc, which is thus not discussed in the present paper (see the 20 – 30 km s $^{-1}$ maps in ranges of $l \sim +44^\circ$ to $+47^\circ$ in Figures 6 and 7 of Su et al. 2019). Figure 9 displays an example for the distance estimation of a part of MC G044.0–02.5, which is consistent with the distance of the whole filamentary MC. Details of the method and an explanation of the figure can be found in Yan et al. (2019).

All of these new results, together with other similar studies (e.g., see Table 3 and Figure 7 in Herczeg et al. 2019), remarkably refine our knowledge on the local MCs. More recently, a narrow and elongated arrangement of dense gas in the local ISM is well unveiled based on the accurate distances of star forming regions toward the anticenter of the Milky Way (Alves et al. 2020). We hope that our study will be helpful in revealing possible large-scale structures toward the inner Galaxy in the future.

3.3. The Mass Distribution of the Local Molecular Gas

After combining the MWISP CO data and more accurate distances of the MCs within $\lesssim 1$ kpc, we can discuss the mass distribution of the local molecular gas toward the Aquila Rift region.

For CO observations, the column density of MCs can be estimated from the ^{12}CO luminosity and the CO-to- H_2 conversion factor, X_{CO} . The total mass of the molecular gas can be calculated if we know the MC’s distance. Usually, the value of $2 \times 10^{20} \text{ cm}^{-2} (\text{K km s}^{-1})^{-1}$ is recommended by many studies (e.g., Dame et al. 2001; Bolatto et al. 2013). Based on the MWISP data, in fact, the conversion factor can be estimated from the ^{12}CO and ^{13}CO emission. And then we can use the estimated value of X_{CO} to calculate the mass of the local MCs.

Here, we use samples of MC G044.5–02.0 to estimate the value of X_{CO} due to little velocity confusion in the direction (see Section 3.4.3). First, assuming that the ^{12}CO emission is optically thick and the beam filling factor of the extended gas is

1, we can estimate the excitation temperature from the peak temperature of ^{12}CO emission. Second, the column density of ^{13}CO is calculated pixel by pixel in the local thermodynamic equilibrium (LTE) assumption (see discussions and equations in Section 3.1.2 of [Su et al. 2015](#)). Third, the column density of H_2 can be obtained by adopting $[^{12}\text{CO}]/[^{13}\text{CO}]=66$ ([Giannetti et al. 2014](#)) and $[\text{H}_2]/[^{12}\text{CO}]\sim 1.7 \times 10^4$. The value of X_{CO} is thus calculated from the resulting ratio between $N(\text{H}_2)$ from the ^{13}CO emission and I_{CO} from the corresponding ^{12}CO data. The mean value of the X-factor is $\sim 2 \times 10^{20} \text{ cm}^{-2}(\text{K km s}^{-1})^{-1}$ under the above assumptions. We find that the $N(\text{H}_2)/I_{\text{CO}}$ vs. I_{CO} trend from MC G044.5–02.5 is similar to the recent result from the Galactic cluster-forming molecular clumps (i.e., see details in [Barnes et al. 2018](#)). We emphasize, however, that the derived value of X_{CO} largely depends on the uncertainties of the abundance ratios of $[^{12}\text{CO}]/[^{13}\text{CO}]$ and $[\text{H}_2]/[^{12}\text{CO}]$, which are difficult to estimate just based on the MWISP CO data.

The MC distances and masses, together with other physical parameters, are briefly summarized in Table 1. The two largest concentrations are W40b and the GMC complex G036.0+01.0, which have a total mass of $\gtrsim 3.4 \times 10^5 M_\odot$. The former is related to the embedded star-forming regions of the H II region W40 and Serpens NE cluster, while the latter region is less studied in the literature. The distance separation between the two main mass concentrations is about 130 pc, which is roughly twice the extension of the GMC complex G036.0+01.0 (i.e., $6^\circ 8' \approx 70$ pc at a mean distance of ~ 610 pc). Other local MCs with $\sim 10^3 - 10^4 M_\odot$ are either in distinct groups (Figures 5 and 8) or in a single concentration (Figure 6).

All of these show that molecular gas toward the Aquila Rift region is distributed in different distances, which agrees well with the new results from the very recent study (see details in [Herczeg et al. 2019](#)). As shown in Figure 7 of [Herczeg et al. \(2019\)](#), the ~ 350 –480 pc for the cyan circles matches our value of ~ 474 pc for the molecular gas toward the W40b region (the middle panel in Figure 5) and the $\gtrsim 550$ pc for the red circles agrees with the value of ~ 560 –670 pc toward the GMC complex G036.0+01.0 (Figure 7). The distance of ~ 235 pc for the molecular gas at the W40a region (left panel in Figure 5) is also consistent with the value of ~ 250 pc for the extended dust cloud (i.e., the Serpens Cirrus, see Table 3 and the yellow contour in Figure 7 of [Herczeg et al. 2019](#)). Moreover, the distance of ~ 404 pc toward the MC G044.0–02.5 (Figure 8) is also consistent with their estimated value of ~ 407 pc for the associated cloud LDN 673 (see Table 1 in [Herczeg et al. 2019](#)).

Toward the Aquila Rift, we conclude that the dominant mass (i.e., $\gtrsim 95\%$) of the local MCs in the coverage is in regions $\gtrsim 400$ pc, while only several $10^3 M_\odot$ MCs are located in regions of $\lesssim 300$ pc. We plan to build a sample database of local MCs with more reliable properties in the next study (e.g., MC identification, distance estimation, and mass distribution, etc.). The MWISP CO data from further accumulation (e.g., $l \sim 20^\circ - 26^\circ$), together with the future releases from the Gaia data, are helpful in studying the properties of the whole local molecular gas.

3.4. Individual Regions

In this Section, we discuss the physical properties of the local MCs with three regions as examples: molecular gas in $l \sim +26^\circ$ to $+33^\circ$, GMC complex G036.0+01.0 in $l \sim +32^\circ$ to $+41^\circ$, and MC G044.0–02.5 in $l \sim +40^\circ$ to $+50^\circ$. We mainly focus on the molecular-gas distribution with different LSR velocities and the dynamical features of the local molecular gas.

3.4.1. MCs toward $l \sim +26^\circ$ to $+33^\circ$ Regions

Figure 10 displays the ^{13}CO emission in the velocity intervals of $[4.5, 7.0] \text{ km s}^{-1}$ (blue), $[7.0, 9.5] \text{ km s}^{-1}$ (green), and $[9.5, 12.0] \text{ km s}^{-1}$ (red). The molecular gas in the velocity range of $4.5\text{--}12.0 \text{ km s}^{-1}$ is mainly located at $\sim 470 \text{ pc}$, excluding some CO gas at $V_{\text{peak}} \sim 2\text{--}4 \text{ km s}^{-1}$ (or $\sim 240\text{--}260 \text{ pc}$ in the left panel of Figure 5).

Toward this region, we find that ^{13}CO emission is a good tracer for identifying MC structures due to its relatively larger extension compared to the C^{18}O emission and its smaller optical depth (Section 3.1) compared to the ^{12}CO emission. Interestingly, at least tens of filaments (the elongated structure with an aspect ratio larger than ~ 5) with different velocity structures are found to be located in the complex region of ^{13}CO emission (see some typical filaments indicated by arrows in Figure 10). The typical length and width of these filamentary structures are tens of arcminutes and several arcminutes, respectively. Additionally, the typical column density of these filaments is in the range of $\sim 10^{21} - 10^{22} \text{ cm}^{-2}$ estimated from the ^{13}CO gas. Several filamentary structures with somewhat different velocities seem to just overlap on the Serpens NE region, which is also seen by Nakamura et al. (2017) according to ^{12}CO ($J=2\text{--}1$) and ^{13}CO ($J=2\text{--}1$) data. Systematic analysis of these filaments will be presented in future works by using some algorithms on the 3D ^{13}CO and C^{18}O data cubes (e.g., see discussions in Xiong et al. 2017, 2019).

We note that the C^{18}O emission is roughly concentrated in these filamentary structures (white contours associated with the filamentary structures in Figure 10). Here, we use PV diagrams (Figure 11) to show the detailed velocity structures of ^{13}CO and C^{18}O emission along two filaments (see red arrows in Figure 10). Including the main velocity structure seen in ^{13}CO and C^{18}O emission (i.e., $V_{\text{LSR}} \sim 6 - 8 \text{ km s}^{-1}$), the ^{13}CO gas also displays additional velocity components (i.e., $V_{\text{LSR}} \sim 3 - 6 \text{ km s}^{-1}$ and $V_{\text{LSR}} \sim 8 - 11 \text{ km s}^{-1}$) near the main LSR velocity structure. In fact, very weak C^{18}O emission (e.g., $T_{\text{peak}18} \lesssim 0.4\text{--}0.5 \text{ K}$ at $\sim 8.5 \text{ km s}^{-1}$ in the right panel of Figure 11) is also found to be associated with this additional velocity structure seen in ^{13}CO emission.

The star formation activities (e.g., Mallick et al. 2013; Nakamura et al. 2014; Dunham et al. 2015; Herczeg et al. 2019) are strong in regions with enhanced C^{18}O emission and the high peak temperature of ^{12}CO gas, e.g., the Serpens NE cluster, the H II region W40, and the H II region Sh 2-62 (or the MWC 297 region at $l = 26.8$ and $b = +3.5$). The most powerful source in this general region is the H II region

W40, which is responsible for the spatial and velocity distributions of the surrounding molecular gas (e.g., see Figures 15–16 and Section 3.3.2 in [Su et al. 2019](#)). On the other hand, the gas in regions with strong C^{18}O emission but relatively low ^{12}CO temperature is probably in such an early stage that star formation is ongoing (e.g., see the Serpens filament and embedded young stellar object (YSO) candidates in [Gong et al. 2018](#)).

Figure 12 displays the gas distribution at ~ 260 pc (the upper panel for MCs G029.0–02.0a) and ~ 400 pc (the lower panel for MCs G030.5–01.5). The CO gas with somewhat different LSR velocities (or distances) has a similar northwest-southeastern extension from $b \sim +0^\circ.5$ to $b \sim -5^\circ.0$ (or with a length of ~ 30 – 50 pc). This finding shows that at least two distinct gas components with different distances are located in the region, which is similar to the W40 region with $b \gtrsim 0^\circ$ (the left and middle panels in Figure 5).

Additionally, many protruding CO structures (see arrows in Figure 12) are located toward a large-scale bright optical nebula centered at ($l \sim 26^\circ$, $b \sim -3^\circ$) with a diameter of several degrees (e.g., see the Southern $\text{H}\alpha$ Sky Survey by [Parker et al. 2005](#)). Some of the CO protrusions, which are perpendicular to the above elongated northwest-southeastern molecular-gas structures, also have remarkable velocity gradients of $\sim 0.7 - 1.3 \text{ km s}^{-1} \text{ pc}^{-1}$ at a distance of ~ 400 pc (e.g., see the black arrow in Figure 13, also see solid lines in Figure 14). Comparing to the quiescent gas at $V_{\text{LSR}} \sim 9$ – 11 km s^{-1} , the ^{12}CO gas near the tip of the protrusion also displays red-shifted velocity up to $\gtrsim 15 \text{ km s}^{-1}$, indicating interactions between the gas and the shock there. We suggest that these features are probably related to nearby stellar feedbacks (e.g., winds and radiation from nearby early-type OB stars or shocks from supernova remnants).

3.4.2. GMC Complex G036.0+01.0

We have shown that the most striking feature in $l \sim +32^\circ$ to $+41^\circ$ is the GMC complex G036.0+01.0 at a distance of ~ 610 pc. The GMC complex has a total mass of $\sim 2.0 \times 10^5 M_\odot$ (Table 1). Similar to other MCs discussed above, filamentary structures and the complex velocity field are also prevalent throughout the GMC complex (Figures 15 and 16). The whole GMC complex, which extends about ~ 35 square degrees in the map, consists of three main parts: the $l \lesssim +36^\circ$ region, the $+36^\circ \lesssim l \lesssim +38^\circ$ region, and the $l \gtrsim +38^\circ$ region (also see Figure 7). These CO clouds, which consist of many arc-like or sub-filamentary structures, display different morphologies in the individual sub-regions of size of ~ 30 – 50 pc.

We made channel maps to show the spatial and velocity distributions of the molecular gas for two sub-regions in the GMC complex (Figures 17 and 18). According to the ^{12}CO channel maps shown in Figure 17, we find that many elongated structures with a length of several tens of arcminutes (or several pc at a distance of ~ 555 pc) and somewhat different LSR velocities (i.e., $\sim 13 - 18 \text{ km s}^{-1}$) are roughly along the

southwest-northeast direction, which is similar to the whole large-scale CO extension in this region (see the arrow in Figure 17).

In the densest region of the GMC complex, the ^{13}CO channel maps reveal several arc-like structures on a scale of $\sim 10 - 20$ pc (e.g., see dashed lines in Figure 18). The large-scale arc-like structures consist of many curved structures with a smaller length of several arcminutes. In fact, these small curved structures can be clearly seen in the channel maps at a velocity separation of 0.2 km s^{-1} due to their coherent spatial and velocity features. C^{18}O emission is concentrated in the large-scale arc-like structures, in which molecular gas displays multi-velocity components revealed by ^{13}CO emission (Figures 16 and 18).

Based on the recent study by Wang et al. (2019), the relatively higher ^{12}CO peak temperature of $\gtrsim 10\text{--}15$ K is usually related to processes of the nearby star formation activities. The peak temperature of the ^{12}CO emission toward the GMC complex is $\lesssim 10$ K (Figure 2). We thus suggest that star formation activities are probably not strong in the surrounding of the GMC complex. We speculate that the GMC complex is likely at an early evolutionary stage when the gas is just accumulating due to the concentrations of the C^{18}O gas in the arc-like structures (see dashed lines in Figure 18). The densest regions traced by the enhanced C^{18}O emission in the GMC (i.e., red contours in Figure 16) are probably good places to investigate the possible star formation activities at the early evolutionary stage.

3.4.3. MC G044.0–02.5

Toward the $l \sim +40^\circ$ to $+50^\circ$ region, the prominent feature of the local molecular gas is the MC G044.0–02.5. The intriguing MC G044.0–02.5 displays a long filamentary structure from ($l \sim +49.7^\circ$, $b \sim -0.9^\circ$, $V_{\text{LSR}} \sim 5.5 \text{ km s}^{-1}$) to ($l \sim +39.5^\circ$, $b \sim -5.1^\circ$, $V_{\text{LSR}} \sim 9.5 \text{ km s}^{-1}$) based on the ^{12}CO emission seen in Figure 19. Roughly, the elongated MC displays some regular CO morphologies: the vortex-like structure in $l \sim [46.7^\circ, 49.5^\circ]$, the plateau structure in $l \sim [45.7^\circ, 47.7^\circ]$, the concave structure in $l \sim [43.4^\circ, 46.1^\circ]$, and the cone structure in $l \sim [39.5^\circ, 43.9^\circ]$ (see labels in Figure 19). The interesting structure has a length of ~ 80 pc and a width of $\sim 7 - 14$ pc in ^{12}CO emission. We stress that the filamentary MC G044.0–02.5 is a single giant molecular filament (GMF) based on its elongated spatial structure and coherent velocity distribution. This is also supported by the distance estimation for the four individual parts of the long filamentary MC (i.e., ~ 400 pc, see Figures 8 and 9).

As seen in Figure 20, the channel maps of ^{12}CO and ^{13}CO emission show that the long MC structure is composed of many sub-filaments with lengths of several arcminutes to tens of arcminutes. Most of the sub-filaments have similar alignments with the long extension of MC G044.0–02.5; although, some tiny elongated structures are also found to be perpendicular to the major axis of the long filamentary cloud (see box regions in the ^{13}CO maps). These velocity-coherent fiber-like structures, which are very thin (i.e., the observed size of $\sim 1' - 2'$ or $\sim 0.1\text{--}0.2$ pc at a distance of 404 pc), tend to converge toward the trunk of the MC traced by the relatively bright

^{13}CO emission along the GMF (e.g., see the box regions in the figure). We named these structures as “networks of tiny filaments or fibers” that are associated with the main trunk of the GMF.

Based on Figure 19, the vortex-like structure centered at ($l \sim +48^\circ.1$, $b \sim -1^\circ.1$, radius $\sim 1'.3$) is prominent at $V_{\text{LSR}} \sim 5 - 6 \text{ km s}^{-1}$. At the southwest of MC G044.0–02.5, a dendritic structure is just across the filamentary MC ($l \sim +40^\circ.6$, $b \sim -4^\circ.4$, $V_{\text{LSR}} \sim 8 - 9 \text{ km s}^{-1}$). The velocity variation of the molecular gas can be clearly seen in the channel maps of CO emission (Figure 20), indicating a systematic velocity gradient of $\sim 0.05 \text{ km s}^{-1} \text{ pc}^{-1}$ along the GMF. This value agrees with the result from analysis of the GMFs in the Milky Way (i.e., $0 - 0.12 \text{ km s}^{-1} \text{ pc}^{-1}$, Ragan et al. 2014; Abreu-Vicente et al. 2016).

In addition to the velocity gradient along the major axis of the filamentary MC (i.e., northeast-southwest), G044.0–02.5 also shows a velocity gradient perpendicular to the major axis of the filament (e.g., $V_{\text{LSR}} \sim 6.0 - 9.5 \text{ km s}^{-1}$ in the $l \sim 42^\circ - 47^\circ$ region; see the red parts of MC G044.0–02.5 in Figure 19). We made PV diagrams across the trunk of the GMF (see arrows in Figure 20). In Figure 21, the PV diagrams show that the velocity gradient perpendicular to the trunk of the GMF is $\sim 0.3 - 0.8 \text{ km s}^{-1} \text{ pc}^{-1}$. The above intriguing scenario is firstly revealed by the large-scale MWISP CO data.

For comparison with other distant MC filaments that are associated with high-mass star-forming regions (e.g., Tackenberg et al. 2014; Dewangan et al. 2018), the $\sim 80 \text{ pc}$ long GMF G044.0–02.5 is situated at the local region and displays abundant details in the spatial and velocity observations discussed above. The relatively low temperature of the molecular gas (i.e., $T_{12\text{COpeak}} \lesssim 10 \text{ K}$) shows that massive star formation activities are probably lacking in the area surrounding the GMF. Many questions need to be investigated for the filamentary cloud, such as the networks of sub-filaments in the GMF, the stability and fragmentation of the long filament, and the star formation in the region.

Figure 22 shows the velocity field of the whole MC. The different spatial features (i.e., vortex, plateau, concave, and cone), as well as the systematic velocity gradients along and perpendicular to the trunk of the GMF, are well revealed by the ^{13}CO emission. According to Figure 23, we find that the dense gas traced by ^{13}CO emission is concentrated in the region with larger ^{12}CO linewidths, indicating high turbulence there (see the red circle in the figure). C^{18}O emission is also enhanced in the region of LDN 673, where many fiber-like structures seem to gather together (see networks of sub-filaments in the upper box of Figure 20).

In fact, the overdensity of YSO candidates from IR data is related to the dense gas region of LDN 673. We also note that the ongoing star formation in their early phase occurs in the densest part of the LDN 673 cloud (e.g., the discovery of many Herbig-Haro objects in LDN 673; Rector et al. 2018). Another box region in Figure 20 displays the similar filamentary networks but where little C^{18}O emission is detected (at $l \sim 42^\circ.2$ to $43^\circ.9$, $b \sim -3^\circ.3$ to $-2^\circ.1$, i.e., LDN 645, LDN 647, and LDN 651).

The interesting velocity features of MC G044.0–02.5, as well as the regular molecular-gas structures, are clearly seen in the CO channel maps with the high spatial dynamic range. We find that filamentary structures are prevalent throughout the MC from scales of several arcminutes to $\gtrsim 10^\circ$. These interesting elongated features are present in particular integrated maps with velocity intervals of $\sim 1\text{--}2\text{ km s}^{-1}$, suggesting the rapid velocity change on a small scale of several arcminutes (Figure 20). For both the ^{12}CO emission and the ^{13}CO emission, in fact, the velocity channel maps show more filamentary structures than the integrated emission maps. Some striation-like features can also be discerned in the channel maps, which is similar to the cases of other nearby MCs (e.g., Goldsmith et al. 2008; Cox et al. 2016; Heyer et al. 2016).

The dust emission (e.g., see OBSID of 1342230842 and 1342230843 from the *Herschel* data) shows similar sub-filaments in the region of LDN 673 centered at ($l \sim 46^\circ 4$, $b \sim -1^\circ 3$). Therefore, we suggest that these tiny features seen in CO emission are real density structures because of the good correlation between the dust emission features and the enhanced ^{13}CO and/or C^{18}O emission. Additionally, these sub-structures in individual velocity channels partly reveal the velocity field of the CO gas, which is useful for investigating the dynamic features of the molecular gas. Moreover, the long MC G044.0–02.5 is also an excellent laboratory to study the large-scale dynamical properties of the molecular gas because of the relatively regular gas morphology, the systematic CO velocity structure, and little cloud confusion in the same direction. We believe that MC G044.0–02.5 is accumulating gas and is in an early evolutionary stage (see Section 3.5).

3.5. MC Formation by Large-scale Converging Flows?

The new CO data show that the local molecular gas is widely spread across the whole map. However, the dominant molecular gas is concentrated in localized regions with complicated velocity fields, i.e., the W40 region, the GMC complex G036.0+01.0, and MC G044.0–02.5 (see Section 3.4). Toward some gas concentrations, MCs with somewhat different LSR velocities often have similar extensions and structures (e.g., see MCs elongated along the northwest-southeast in Figure 12 and large-scale arc-like structures in Figure 18). These large-scale MC concentrations are highly structured and organized, as well as those hierarchical sub-structures within them (also see filamentary networks in box regions of Figure 20). With these details in mind, we wonder how the MCs are formed in the local ISM.

In theoretical studies, MCs may form out of large-scale converging atomic gas flows, which probably originate from shocks by stellar feedback processes (e.g., expansion of H II regions, winds of early-type stars, and explosion of supernovae), as well as large-scale gravitational instability and shear motions. These mechanisms can produce compressive flows and drive large-scale turbulence into the ISM. Turbulence, thermal instability, and local gravitational instability may be responsible for the density

fluctuations, leading to the dense gas formation out of the diffuse atomic hydrogen. Several theoretical views on the topic are discussed by some authors (e.g., [Hennebelle & Falgarone 2012](#); [Dobbs et al. 2014](#); [Klessen & Glover 2016](#)). Additionally, many numerical studies on MC formation have also been undertaken recently (e.g., [Koyama & Inutsuka 2000](#); [Dobbs et al. 2006](#); [Heitsch et al. 2005, 2006, 2008](#); [Hennebelle et al. 2008](#); [Vázquez-Semadeni et al. 2006, 2007](#); [Glover et al. 2010](#); [Smith et al. 2014](#)).

Therefore, large-scale gas flows are ubiquitous in the ISM due to the energy input by activities of massive stars or Galactic shearing motions. Such large-scale gas flows, which probably play a crucial role in accumulating the large amount of gas material, may display some observational features in multi-wavelengths. We speculate that the systematic velocity structure seen in CO emission is one piece of the observational evidence for large-scale flows.

For example, the intriguing case of MC G044.0–02.5 displays the systematic velocity structure along and perpendicular to the major axis of the ~ 80 pc long filament (Figures 19–22), which probably indicates the large-scale gas flows in the local ISM. Based on Section 3.4, we note that the dense gas of the MC often displays multi-velocity components, which can also be found in other regions (e.g., see contours in Figure 11 and channel maps of Figure 18). These features seem to support the idea that the gas is converging in the localized region of the MC, although the correlation between the dense gas concentrations and the multi-velocity components needs to be further investigated for the whole mapping region.

In the following paragraphs, we focus on the observational points of the formation of MC G044.0–02.5 based on (1) the relationship between HI atomic gas and CO molecular gas, (2) the coherent spatial structures of MCs on various scales, and (3) the regular dynamical features of gas from its velocity field.

A large amount of atomic gas traced by enhanced HI emission from the Arecibo data is found to be associated with MC G044.0–02.5 because of the similar spatial morphology and velocity structure between them (Figure 24). In fact, the large-scale structure of the atomic gas extends to ($l \sim 37^\circ.5$, $b \sim -6^\circ.5$), which is not covered by the current MWISP CO map. Based on Figure 24, we find that the CO emission of the intriguing structure appears in the overlapping HI gas regions, i.e., the yellow parts of $6\text{--}9\text{ km s}^{-1}$ (green) and $9\text{--}11\text{ km s}^{-1}$ (red) in the map. Along the directions indicated by cyan arrows in the figure, the atomic gas displays a similar velocity gradient perpendicular to the main trunk of the CO structure (i.e., the HI gas from the green color of $6\text{--}9\text{ km s}^{-1}$ to the red color of $9\text{--}11\text{ km s}^{-1}$; also see the velocity trend of CO gas in Figure 21). On a larger scale, the velocity trend of the atomic gas also shows such the velocity gradient from the northwest to the southeast, which is comparable to the velocity structure of the CO gas (Figure 19). This feature probably indicates the transition from the converging atomic gas to newborn molecular gas on large scales.

In Section 3.4.3, we show that the long MC G044.0–02.5 has different morphologies on scales of $\sim 2^\circ - 4^\circ$ (or $\sim 10\text{--}30$ pc; see Figure 19). The gas in these sub-regions also exhibits regular networks organized by tiny CO sub-filaments or fibers, which have somewhat different but coherent velocity features (Figure 20). The different gas structures in these sub-regions are probably the result of the localized feedback of star formation or various instabilities of the gas flow in the ISM (e.g., gravitation, magnetic field, and thermal pressure).

The denser gas traced by ^{13}CO and C^{18}O emission is often located in regions of filamentary networks (see box regions in Figure 20). CO emission of these coherent structures frequently shows asymmetric line profiles or multi-velocity components rather than a single Gaussian profile (e.g., see PV diagrams in Figure 21), possibly indicating the assembling gas in certain regions. Similar features were also revealed by some authors in simulations (e.g., Heitsch et al. 2009; Smith et al. 2014) and observations (e.g., Su et al. 2017; Wang et al. 2017; Dhabal et al. 2018). For the particular case of LDN 673, the gas seems to converge toward the hub-like region (see the upper box region in Figures 20 and 22), in which the ^{13}CO emission is embedded in the enhanced ^{12}CO emission with broader linewidths (the red circle in Figure 23). The dense C^{18}O gas is spatially associated with the concentration of the ^{13}CO emission with multiple velocity structures (Figure 22). These characteristics probably indicate that molecular gas is also assembling in sub-regions of MC G044.0–02.5, supporting the idea of the simultaneous piling up of material in the whole cloud of ~ 100 pc and some localized regions of several pc.

We suggest that MC G044.0–02.5 forms from large-scale atomic flows, which provide a natural mechanism to accumulate material in large-scale regions of ~ 100 pc. We find that bundles of tiny filaments or networks of fiber-like structures are ubiquitous in the MWISP CO maps. These elongated structures can be naturally explained by turbulent flows, which will lead to gas concentration and subsequent fragmentation on scales of ~ 0.5 pc (i.e., at least five times of the beamwidth) to several pc.

We also note that the magnetic field from the *Planck* 353 GHz data is roughly aligned with the long filament (Figure 25). This fact shows that the magnetic field may play an important role in the formation of the molecular-gas structure, which needs to be investigated by further observations and simulations (e.g., see cases in Pattle et al. 2017; Li & Klein 2019).

Taken as a whole, MCs may form from the pre-existing atomic gas, in which large-scale converging flows may be crucial for the accumulation of material. When atomic gas is assembled by large-scale converging flows, collision between these filamentary flows becomes inevitable and will lead to gas compression. Furthermore, in the environment of pressure enhancement by colliding flows, MC formation is probably rapid due to dynamical processes (e.g., Koyama & Inutsuka 2000; Bergin et al. 2004; Glover & Mac Low 2007; Glover et al. 2010; Su et al. 2018) and various instabilities (e.g., Hennebelle & Falgarone 2012; Dobbs et al. 2014; Klessen & Glover 2016). This sce-

nario indicates that MCs are likely evolving transient objects from filamentary HI gas to H₂ gas and then MCs traced by observed CO emission (e.g., Blitz et al. 2007; Hennebelle et al. 2008).

We find a good coincidence between the emergence of the overdensity of YSO candidates and the concentrations of enhanced C¹⁸O emission (see Section 3.4.3 and Figure 22), suggesting that star formation at their early evolutionary stages occurs in the densest part of the forming cloud. This is consistent with the suggestion that star formation is probably rapid within one or two crossing times in the localized dense regions of MCs (e.g., Elmegreen 2000; Heitsch & Hartmann 2008; also see Hartmann et al. 2001; Pringle et al. 2001; Elmegreen & Scalo 2004; Elmegreen 2007).

4. SUMMARY

We have analyzed molecular line observations of ¹²CO, ¹³CO, and C¹⁸O ($J=1-0$) emission toward the Aquila Rift region by using the Delingha 13.7 m telescope. The whole CO mapping, which is obtained as part of the MWISP project, covered a ~ 250 deg² areas with a grid spacing of 30'' toward the Aquila Rift region. The sensitive molecular line data, together with their high spatial dynamic range mapping, allowed us to investigate the details of the local molecular gas traced by CO emission. Our main results are summarized below.

1. In the covered region of $l = 25^\circ.8-49^\circ.7$ and $|b| \lesssim 5^\circ.2$, CO emission exhibits large-scale extended structures for the local MCs within an LSR velocity range of $-5 \text{ km s}^{-1} \lesssim V_{\text{LSR}} \lesssim +25 \text{ km s}^{-1}$. About half of the covered region has ¹²CO emission, while C¹⁸O emission is only located in the densest region, which is usually associated with star formation activities. The ¹³CO emission, which is embedded in the extended ¹²CO layer, is found to be a good tracer of the main structure of the local MCs.

2. Our new data have revealed many molecular-gas structures traced by weak ¹²CO emission, which cannot be discerned by previous CO surveys because of their relatively low resolution and sensitivity. The dominant region of the local MCs is occupied by such the weak ¹²CO emission, with a low peak temperature of $\lesssim 4.5$ K (i.e., ~ 7.8 K for excitation temperature), indicating subthermal excitation in the low-H₂-density environment.

3. Toward the Aquila Rift region, large-size MC structures are identified from ¹²CO emission in coherent spatial and velocity distributions. In combination with the MWISP CO data and the Gaia DR2, distances of these local molecular-gas structures are well determined in the range of $\sim 200-800$ pc (Figures 5–8 and Table 1) through Bayesian analysis and an MCMC algorithm. The dominant mass of the local molecular gas is in the W40 region and the GMC complex G036.0+01.0, both of which are located at a distance of $\gtrsim 470$ pc.

4. For the W40 region, two overlapping molecular-gas components with similar extensions are located at different distances of ~ 235 pc and ~ 474 pc, respectively.

The ~ 474 pc MCs are associated with its surrounding star formation activities, i.e., Sh 2–62, H II region W40, and Serpens NE Cluster. Generally, in regions of $l \sim +26^\circ$ to $+33^\circ$, the $\lesssim 240$ – 260 pc MCs with lower gas masses have spatial distributions from the northwest to the southeast, which are similar to the results of the extended dust clouds at ~ 250 pc (i.e., the Serpens Cirrus in front of the star-forming region of W40, [Herczeg et al. 2019](#)).

5. The $\sim 2.0 \times 10^5 M_\odot$ GMC complex G036.0+01.0, which is less studied in the literature, consists of several molecular-gas components at a distance range of ~ 560 – 670 pc. Along that direction, some smaller MCs at ~ 220 – 240 pc appear to be in front of the GMC complex (Figures 6 and 7). These nearer MCs at ~ 220 – 240 pc are widely distributed in the whole mapping region, although the mass of the molecular gas is generally small, i.e., $\sim 10^2 - 10^3 M_\odot$.

6. In regions with a larger Galactic longitude, the main MC structure is GMF G044.0–02.5, which has a mass of $\sim 2.4 \times 10^4 M_\odot$ and is located at a distance of ~ 404 pc (Figure 8). Due to a little confusion between different cloud components in the region, the long filamentary MC becomes a good target to study the detailed spatial and velocity structures of the molecular gas from several arcminutes to ten degrees (or ~ 0.5 pc to tens of pc). The ~ 80 pc long MC G044.0–02.5 appears to be surrounded by more extended filamentary HI gas that has a similar spatial structure and velocity gradient to that seen in the CO emission, indicating that the molecular gas is probably forming from large-scale atomic gas. Interestingly, the dense gas of the MC is often located in enhanced CO regions with asymmetric line profiles or multi-velocity components.

7. These characteristics from the new CO data suggest that material accumulation, together with localized gas dynamics and various instabilities, is essential for the formation and evolution of MCs. We suggest that the MCs toward the Aquila Rift region are likely formed by large-scale converging HI flows in the local ISM. This mechanism can naturally explain the rapid MC formation and simultaneous star formation in localized dense regions. In fact, we note that the ongoing star formation occurs in the densest part of the MC G044.0–02.5 (i.e., the overdensity of YSO candidates and groups of HH objects in LDN 673 at $l = 46^\circ 26'$, $b = -1^\circ 33'$).

We gratefully acknowledge the staff members of the Qinghai Radio Observing Station at Delingha for their support in obtaining the observations. We would like to thank the anonymous referee for carefully reading through the manuscript and, we appreciate the many constructive comments and suggestions that improved the paper. MWISP is funded by the National Key R&D Program of China (2017YFA0402700) and the Key Research Program of Frontier Sciences of CAS (QYZDJ-SSW-SLH047). Y.S. is supported by the NSFC grant No. 11773077. X.C. acknowledges support by the NSFC through grant No. 11629302.

This work has made use of data from the European Space Agency (ESA) mission Gaia (<https://www.cosmos.esa.int/gaia>), processed by the Gaia Data Processing and Analysis Consortium (DPAC, <https://www.cosmos.esa.int/web/gaia/dpac/consortium>). Funding for the DPAC has been provided by national institutions, in particular the institutions participating in the Gaia Multilateral Agreement.

This publication utilizes data from the Galactic ALFA HI (GALFA HI) survey data set obtained with the Arecibo *L*-band Feed Array (ALFA) on the Arecibo 305 m telescope. The Arecibo Observatory is part of the National Astronomy and Ionosphere Center, which is operated by Cornell University under Cooperative Agreement with the U.S. National Science Foundation. The GALFA HI surveys are funded by the NSF through grants to Columbia University, the University of Wisconsin, and the University of California.

Facility: PMO 13.7m

Software: GILDAS/CLASS (Pety 2005)

REFERENCES

- Abreu-Vicente, J., Ragan, S., Kainulainen, J., et al. 2016, *A&A*, 590, A131
- Alves, J., Zucker, C., Goodman, A. A., et al. 2020, *Nature*, 578, 237
- Barnes, P. J., Hernandez, A. K., Muller, E., & Pitts, R. L. 2018, *ApJ*, 866, 19
- Barnes, P. J., Muller, E., Indermuhle, B., et al. 2015, *ApJ*, 812, 6
- Bergin, E. A., Hartmann, L. W., Raymond, J. C., & Ballesteros-Paredes, J. 2004, *ApJ*, 612, 921
- Blitz, L., Fukui, Y., Kawamura, A., et al. 2007, in *Protostars and Planets V*, ed. B. Reipurth, D. Jewitt, & K. Keil, 81
- Bolatto, A. D., Wolfire, M., & Leroy, A. K. 2013, *ARA&A*, 51, 207
- Burton, M. G., Braiding, C., Glueck, C., et al. 2013, *PASA*, 30, e044
- Cox, N. L. J., Arzoumanian, D., André, P., et al. 2016, *A&A*, 590, A110
- Dame, T. M., Hartmann, D., & Thaddeus, P. 2001, *ApJ*, 547, 792
- Dame, T. M., & Thaddeus, P. 1985, *ApJ*, 297, 751
- Dame, T. M., Ungerechts, H., Cohen, R. S., et al. 1987, *ApJ*, 322, 706
- Dewangan, L. K., Baug, T., Ojha, D. K., Zinchenko, I., & Luna, A. 2018, *ApJ*, 864, 54
- Dhabal, A., Mundy, L. G., Rizzo, M. J., Storm, S., & Teuben, P. 2018, *ApJ*, 853, 169
- Dobbs, C. L., Bonnell, I. A., & Pringle, J. E. 2006, *MNRAS*, 371, 1663
- Dobbs, C. L., Krumholz, M. R., Ballesteros-Paredes, J., et al. 2014, in *Protostars and Planets VI*, ed. H. Beuther, R. S. Klessen, C. P. Dullemond, & T. Henning, 3
- Dunham, M. M., Allen, L. E., Evans, Neal J., I., et al. 2015, *ApJS*, 220, 11
- Elmegreen, B. G. 2000, *ApJ*, 530, 277
- . 2007, *ApJ*, 668, 1064
- Elmegreen, B. G., & Scalo, J. 2004, *ARA&A*, 42, 211
- Gaia Collaboration, Prusti, T., de Bruijne, J. H. J., et al. 2016, *A&A*, 595, A1
- Gaia Collaboration, Brown, A. G. A., Vallenari, A., et al. 2018, *A&A*, 616, A1
- Giannetti, A., Wyrowski, F., Brand, J., et al. 2014, *A&A*, 570, A65

- Glover, S. C. O., Federrath, C., Mac Low, M.-M., & Klessen, R. S. 2010, *MNRAS*, 404, 2
- Glover, S. C. O., & Mac Low, M.-M. 2007, *ApJ*, 659, 1317
- Goldsmith, P. F., Heyer, M., Narayanan, G., et al. 2008, *ApJ*, 680, 428
- Gong, Y., Li, G. X., Mao, R. Q., et al. 2018, *A&A*, 620, A62
- Hartmann, L., Ballesteros-Paredes, J., & Bergin, E. A. 2001, *ApJ*, 562, 852
- Heitsch, F., Ballesteros-Paredes, J., & Hartmann, L. 2009, *ApJ*, 704, 1735
- Heitsch, F., Burkert, A., Hartmann, L. W., Slyz, A. D., & Devriendt, J. E. G. 2005, *ApJL*, 633, L113
- Heitsch, F., & Hartmann, L. 2008, *ApJ*, 689, 290
- Heitsch, F., Hartmann, L. W., Slyz, A. D., Devriendt, J. E. G., & Burkert, A. 2008, *ApJ*, 674, 316
- Heitsch, F., Slyz, A. D., Devriendt, J. E. G., Hartmann, L. W., & Burkert, A. 2006, *ApJ*, 648, 1052
- Hennebelle, P., Banerjee, R., Vázquez-Semadeni, E., Klessen, R. S., & Audit, E. 2008, *A&A*, 486, L43
- Hennebelle, P., & Falgarone, E. 2012, *A&A Rv*, 20, 55
- Herczeg, G. J., Kuhn, M. A., Zhou, X., et al. 2019, *ApJ*, 878, 111
- Heyer, M., & Dame, T. M. 2015, *ARA&A*, 53, 583
- Heyer, M., Goldsmith, P. F., Yıldız, U. A., et al. 2016, *MNRAS*, 461, 3918
- Heyer, M. H., Brunt, C., Snell, R. L., et al. 1998, *ApJS*, 115, 241
- Klessen, R. S., & Glover, S. C. O. 2016, *Saas-Fee Advanced Course*, 43, 85
- Koyama, H., & Inutsuka, S.-I. 2000, *ApJ*, 532, 980
- Li, P. S., & Klein, R. I. 2019, *MNRAS*, 485, 4509
- Mallick, K. K., Kumar, M. S. N., Ojha, D. K., et al. 2013, *ApJ*, 779, 113
- Nakamura, F., Dobashi, K., Shimoikura, T., Tanaka, T., & Onishi, T. 2017, *ApJ*, 837, 154
- Nakamura, F., Sugitani, K., Tanaka, T., et al. 2014, *ApJL*, 791, L23
- Narayanan, G., Heyer, M. H., Brunt, C., et al. 2008, *ApJS*, 177, 341
- Ortiz-León, G. N., Dzib, S. A., Kounkel, M. A., et al. 2017, *ApJ*, 834, 143
- Ortiz-León, G. N., Loinard, L., Dzib, S. A., et al. 2018, *ApJL*, 869, L33
- Parker, Q. A., Phillipps, S., Pierce, M. J., et al. 2005, *MNRAS*, 362, 689
- Pattle, K., Ward-Thompson, D., Berry, D., et al. 2017, *ApJ*, 846, 122
- Pety, J. 2005, in *SF2A-2005: Semaine de l'Astrophysique Française*, ed. F. Casoli, T. Contini, J. M. Hameury, & L. Pagani, (Les Ulis: EDP), 721
- Planck Collaboration, Ade, P. A. R., Aghanim, N., et al. 2015, *A&A*, 576, A104
- Prato, L., Rice, E. L., & Dame, T. M. 2008, Where are all the Young Stars in Aquila?, ed. B. Reipurth, Vol. 4, 18
- Pringle, J. E., Allen, R. J., & Lubow, S. H. 2001, *MNRAS*, 327, 663
- Ragan, S. E., Henning, T., Tackenberg, J., et al. 2014, *A&A*, 568, A73
- Rector, T. A., Shuping, R. Y., Prato, L., & Schweiker, H. 2018, *ApJ*, 852, 13
- Reid, M. J., Menten, K. M., Brunthaler, A., et al. 2019, *ApJ*, 885, 131
- Shan, W., Yang, J., Shi, S., et al. 2012, *ITTST*, 2, 593
- Smith, R. J., Glover, S. C. O., & Klessen, R. S. 2014, *MNRAS*, 445, 2900
- Su, Y., Sun, Y., Li, C., et al. 2016, *ApJ*, 828, 59
- Su, Y., Zhang, S., Shao, X., & Yang, J. 2015, *ApJ*, 811, 134
- Su, Y., Zhou, X., Yang, J., et al. 2018, *ApJ*, 863, 103
- . 2017, *ApJ*, 836, 211
- Su, Y., Yang, J., Zhang, S., et al. 2019, *ApJS*, 240, 9
- Sun, J. X., Lu, D. R., Yang, J., et al. 2018, *AcASn*, 59, 3
- Sun, Y., Su, Y., Zhang, S.-B., et al. 2017, *ApJS*, 230, 17
- Tackenberg, J., Beuther, H., Henning, T., et al. 2014, *A&A*, 565, A101
- Vázquez-Semadeni, E., Gómez, G. C., Jappsen, A. K., et al. 2007, *ApJ*, 657, 870

- Vázquez-Semadeni, E., Ryu, D., Passot, T., González, R. F., & Gazol, A. 2006, *ApJ*, 643, 245
- Wang, C., Yang, J., Su, Y., et al. 2019, *ApJS*, 243, 25
- Wang, C., Yang, J., Xu, Y., et al. 2017, *ApJS*, 230, 5
- Xiong, F., Chen, X., Yang, J., et al. 2017, *ApJ*, 838, 49
- Xiong, F., Chen, X., Zhang, Q., et al. 2019, *ApJ*, 880, 88
- Yan, Q.-Z., Zhang, B., Xu, Y., et al. 2019, *A&A*, 624, A6
- Zhang, M., Kainulainen, J., Mattern, M., Fang, M., & Henning, T. 2019, *A&A*, 622, A52
- Zucker, C., Speagle, J. S., Schlafly, E. F., et al. 2019, *ApJ*, 879, 125

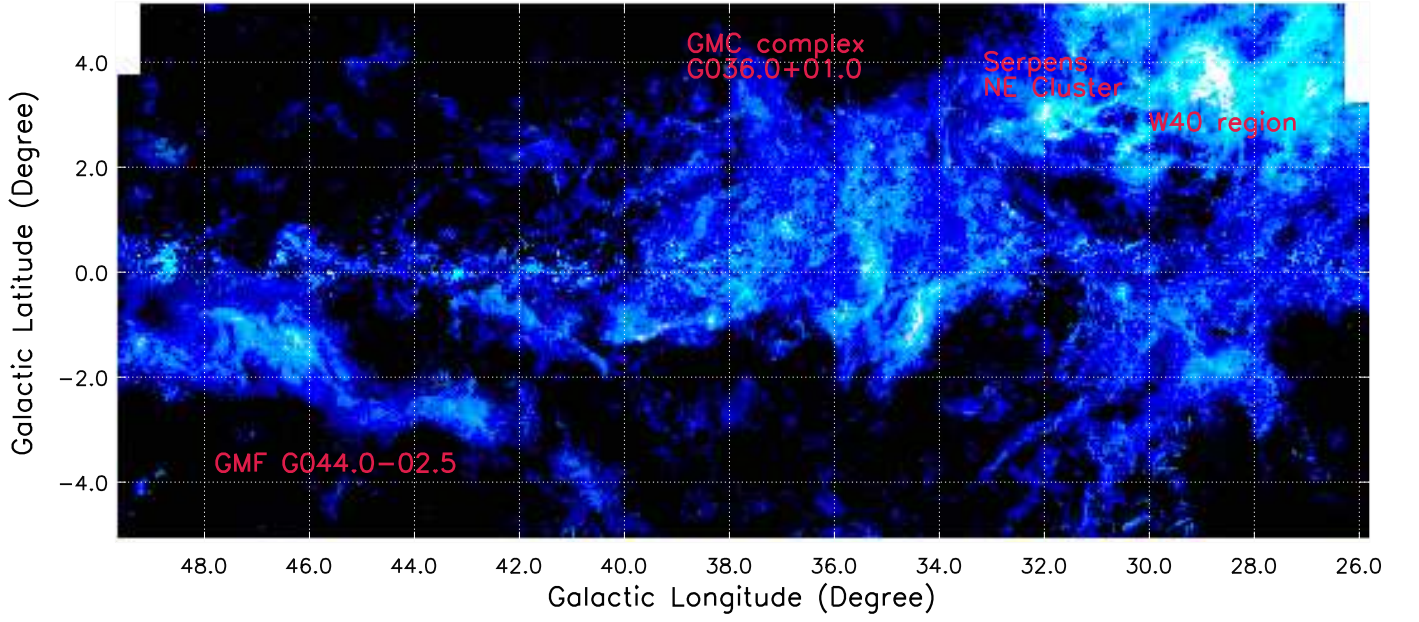


Figure 1. ^{12}CO ($J=1-0$, blue), ^{13}CO ($J=1-0$, green), and C^{18}O ($J=1-0$, red) intensity map in the velocity range of $[-1, 25] \text{ km s}^{-1}$. For subsequent studies, several regions (i.e., W40 region, Serpens NE cluster, GMC complex G036.0+01.0, and GMF G044.0-02.5) are labeled on the map.

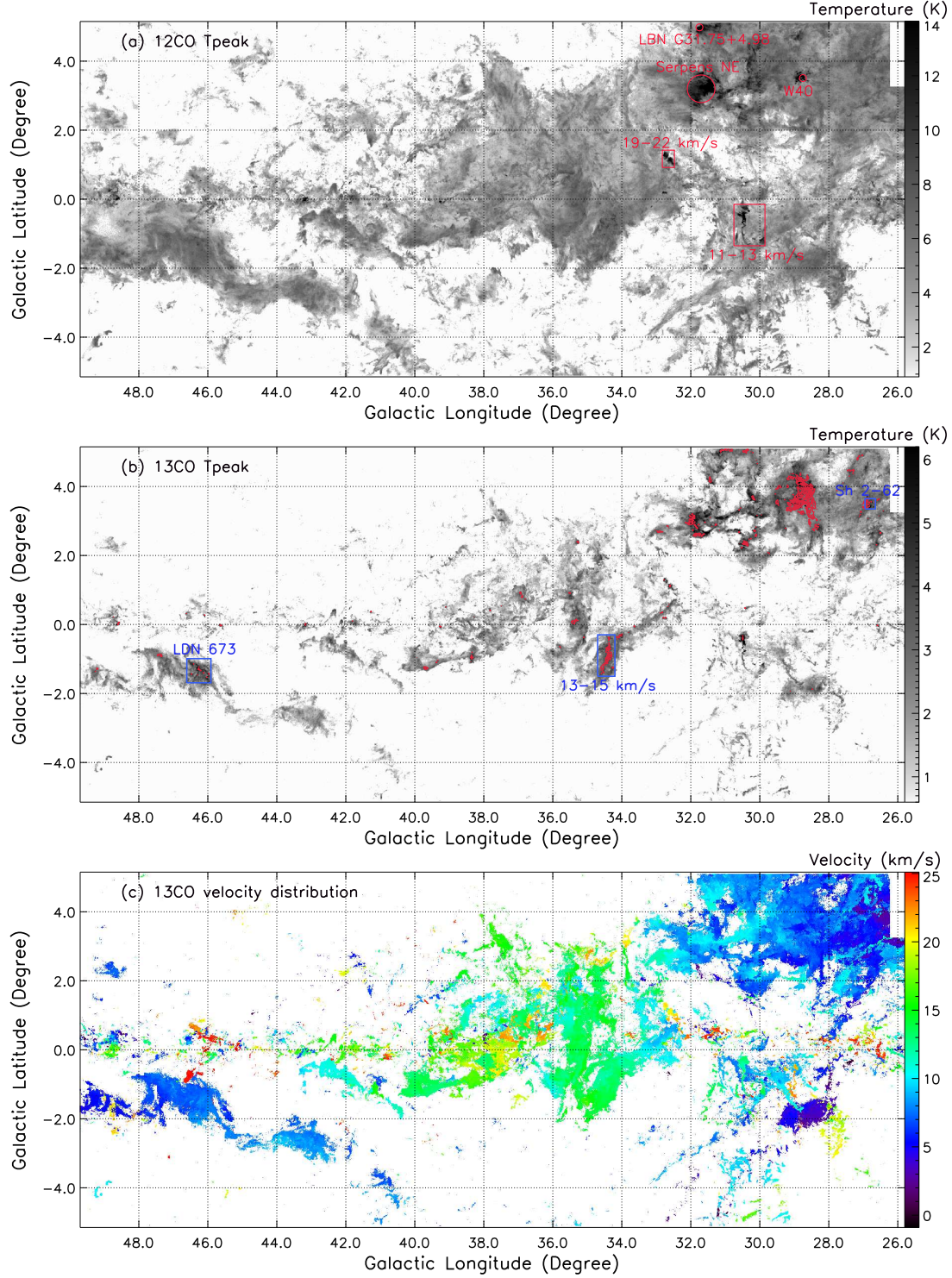


Figure 2. Panel (a): Peak temperature (T_{MB}) of the ^{12}CO emission in the velocity interval of $[-1, 25] \text{ km s}^{-1}$ in the whole region. The three red circles show the known active star-forming regions with $T_{\text{peak}12} \gtrsim 10 \text{ K}$, i.e., W40, Serpens NE Cluster, and LBN 031.75+04.98. The two red rectangles show other regions with high peak temperature of ^{12}CO emission. Panel (b): Peak temperature of the ^{13}CO emission overlaid with the C^{18}O integrated emission contours of 1, 2, 3, and 4 K km s^{-1} (in red). The two blue boxes show the active star-forming regions with $T_{\text{peak}12} \lesssim 10 \text{ K}$, i.e., Sh 2-62 and LDN 673. The blue rectangle shows the C^{18}O concentration at 13–15 km s^{-1} . Panel (c): Intensity-weighted ^{13}CO mean velocity (first moment) map (or the velocity field).

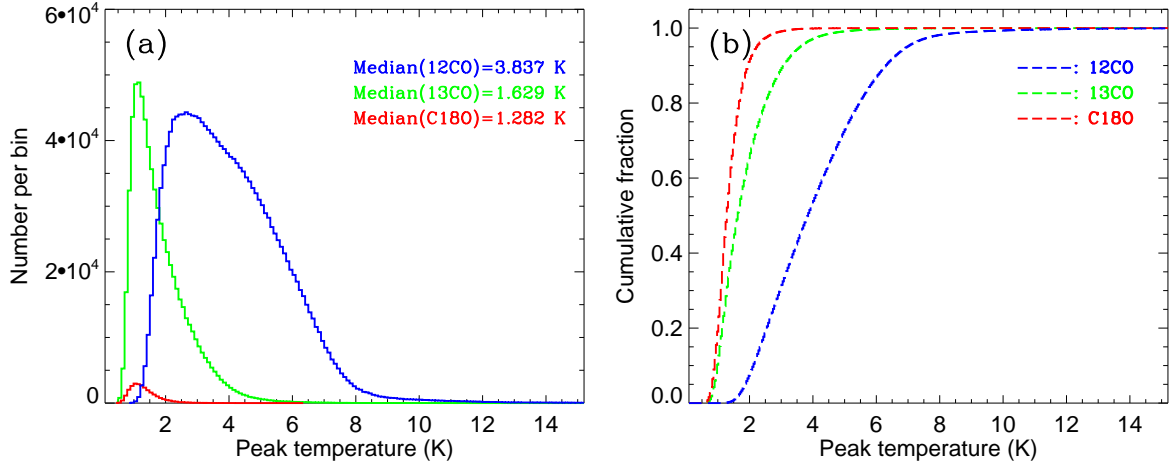


Figure 3. Panel (a): Distribution of the peak temperatures of the three lines for the local molecular gas in the velocity range of $[-1, 25]$ km s^{-1} . The blue, green, and red lines indicate the 1.8×10^6 , 7.0×10^5 , and 2.6×10^4 samples for the ^{12}CO , ^{13}CO , and C^{18}O emission, respectively. Panel (b): Cumulative distribution of peak temperatures for the three CO lines. Note that points with three consecutive channels greater than 3σ are considered to be the valid samples. The total number of pixels in the whole observed region is $\sim 3.5 \times 10^6$.

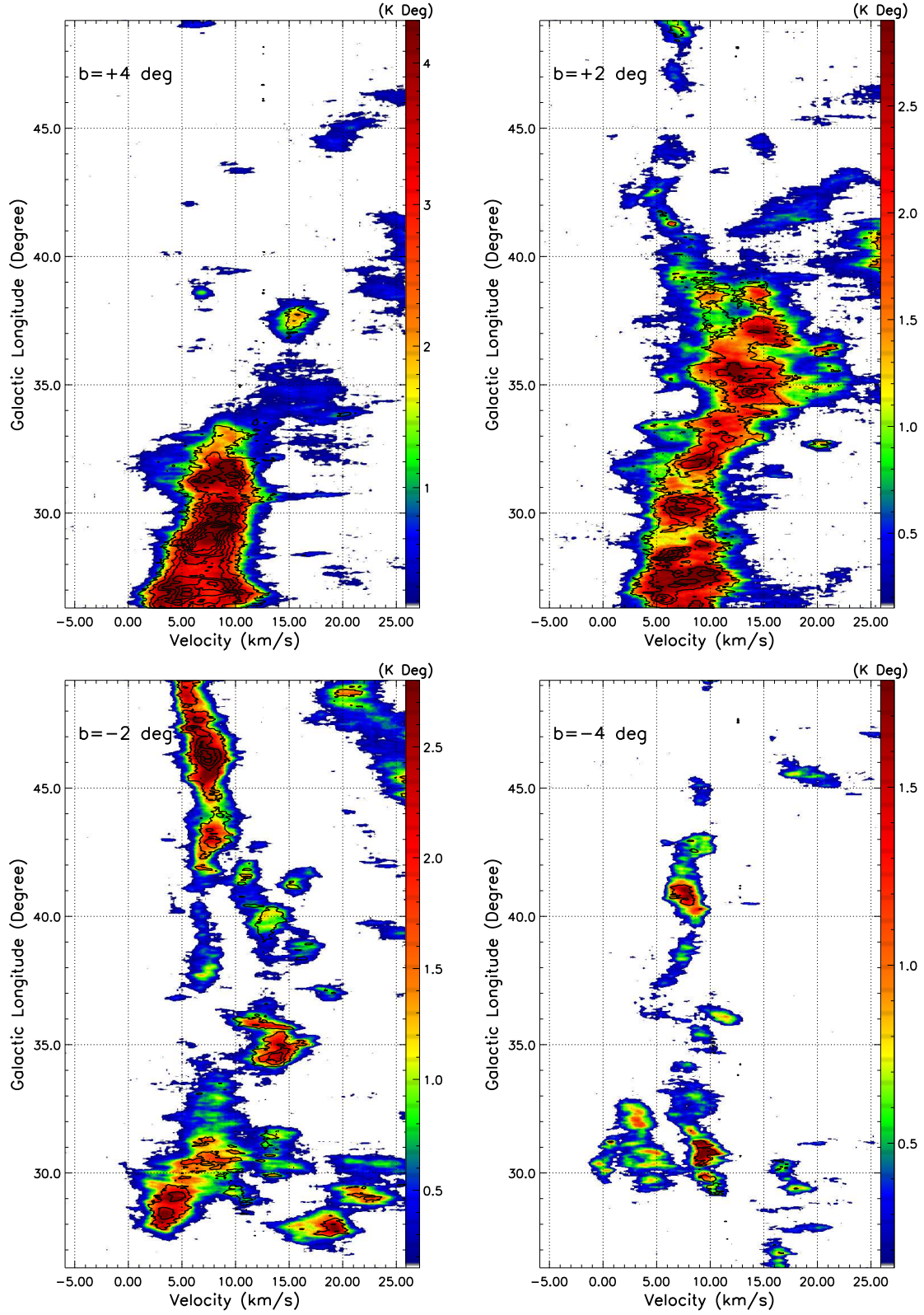


Figure 4. Longitude–velocity diagrams of the ^{12}CO (color) and ^{13}CO (contours) emission for the local molecular gas along $b = +4^\circ$, $+2^\circ$, -2° , and -4° , respectively. The slices have a length of 23.9 and a width of 2.0 . The contours of ^{13}CO emission start from 0.15 K Deg with a step of 0.3 K Deg.

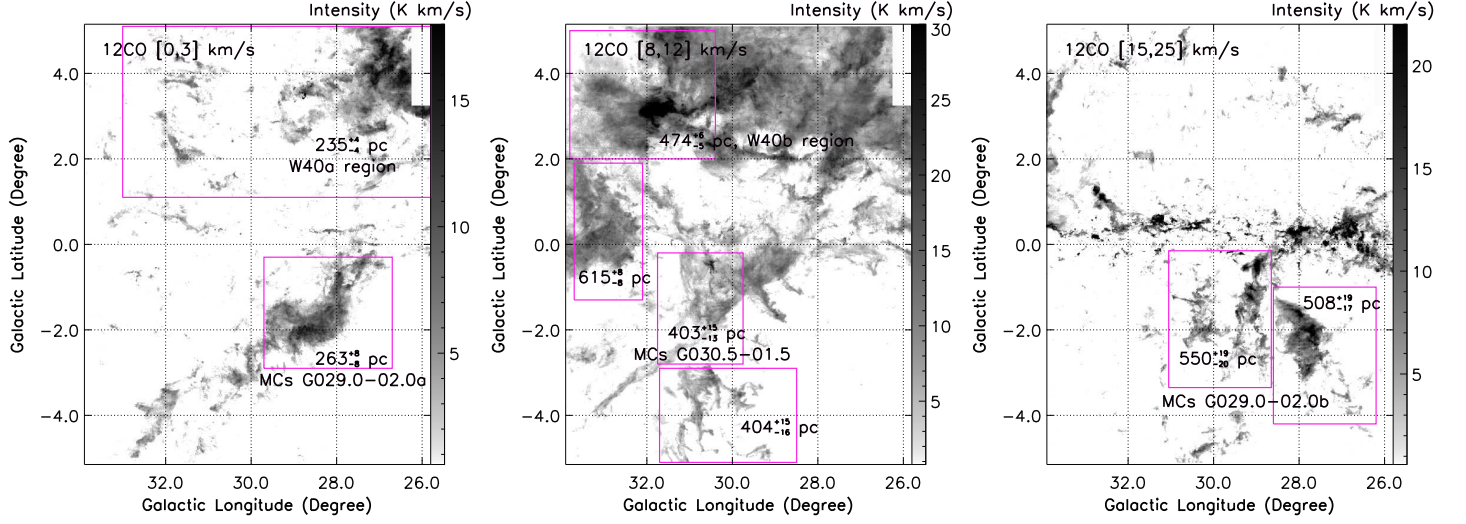


Figure 5. ^{12}CO ($J=1-0$) intensity maps toward $l \sim +26^\circ$ to $+33^\circ$ in the $[0, 3]$, $[8, 12]$, and $[15, 25]$ km s^{-1} , respectively. The distances of the corresponding molecular gas are labeled on the map. Note that distances in the map are estimated for the areas indicated by the rectangles but only using regions with high-integrated CO intensity (see the threshold in the text).

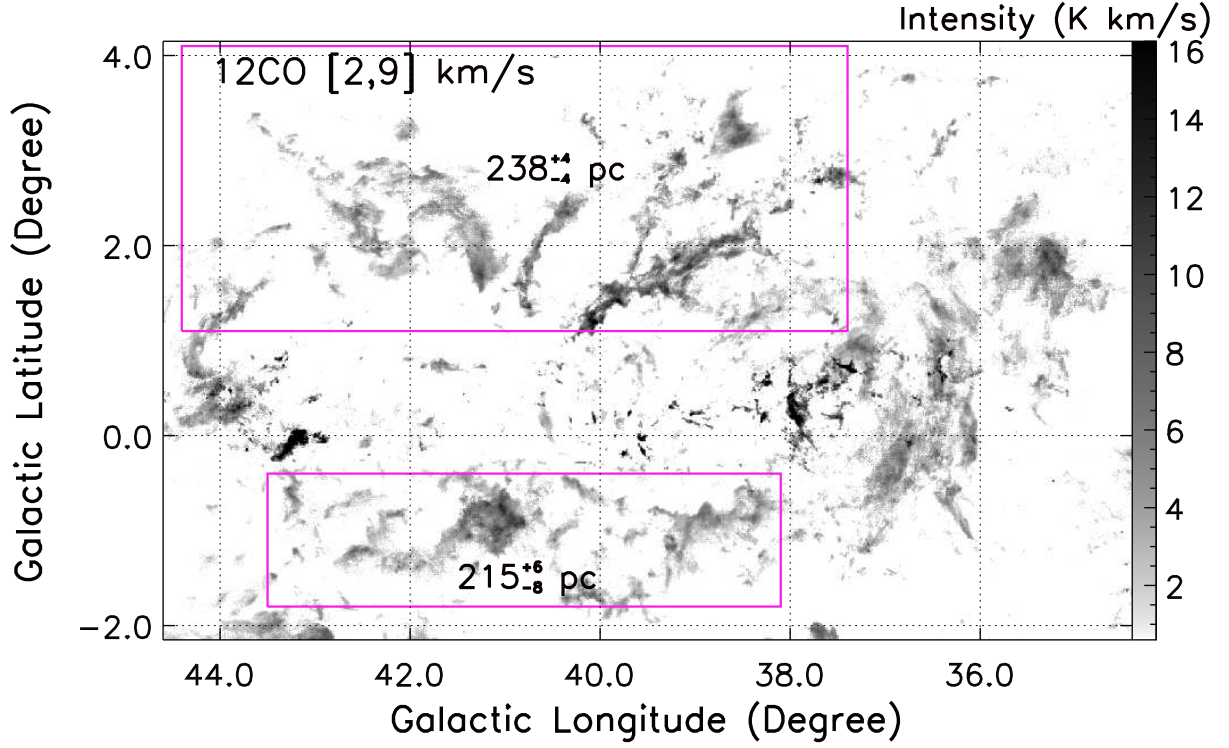


Figure 6. ^{12}CO ($J=1-0$) intensity map toward $l \sim +35^\circ$ to $+44^\circ$ in the $[2, 9] \text{ km s}^{-1}$ interval. The distances of the corresponding molecular gas are labeled on the map. Note that distances in the map are estimated for the areas indicated by the rectangles but only using regions with high-integrated CO intensity (see the threshold in the text). The map also displays many shell-like structures with sizes of several pc.

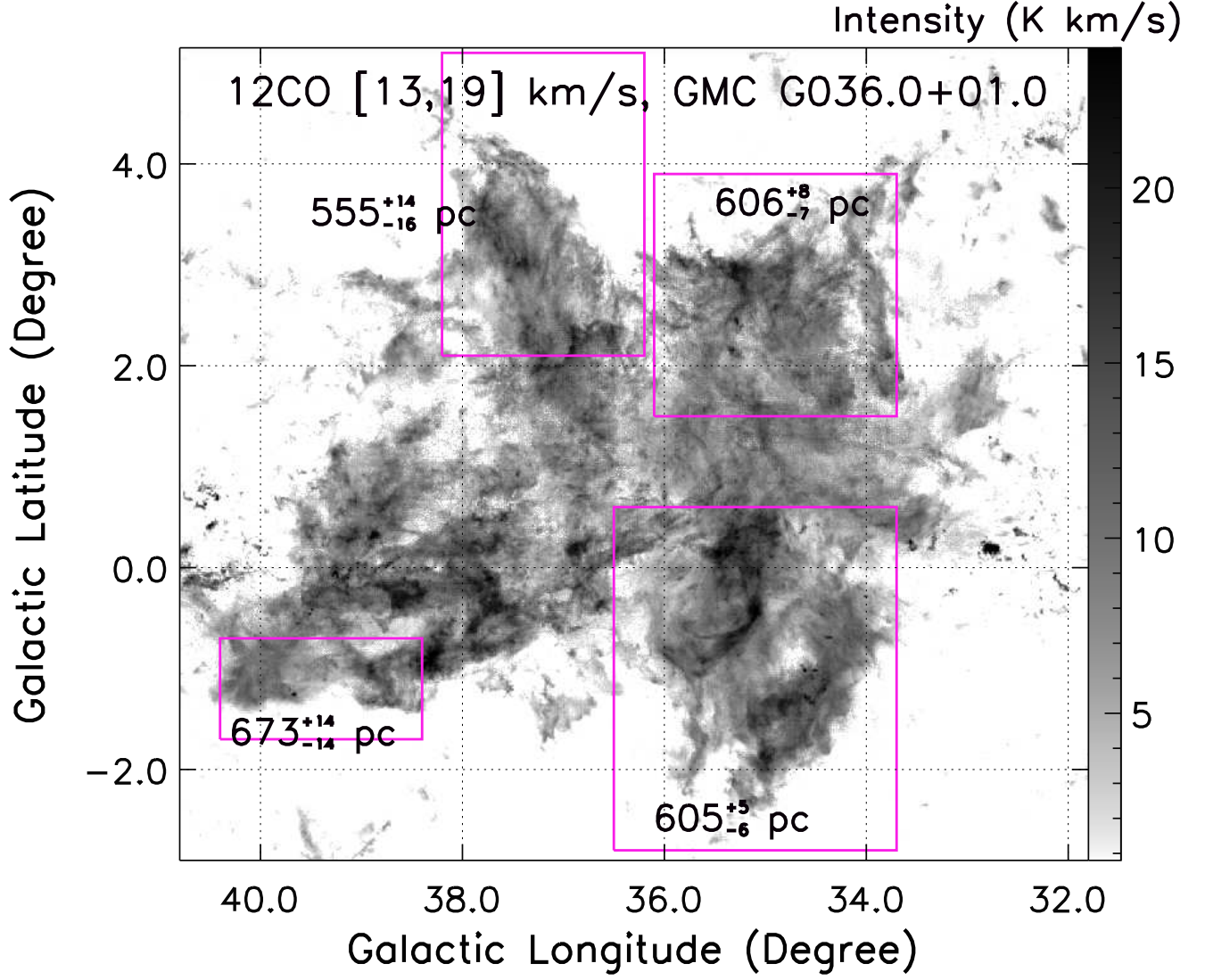


Figure 7. ^{12}CO ($J=1-0$) intensity map toward $l \sim +32^\circ$ to $+41^\circ$ in the $[13, 19]$ km s^{-1} interval. The distances of the corresponding molecular gas are labeled on the map. Note that distances in the map are estimated for the areas indicated by the rectangles but only using regions with high-integrated CO intensity (see the threshold in the text).

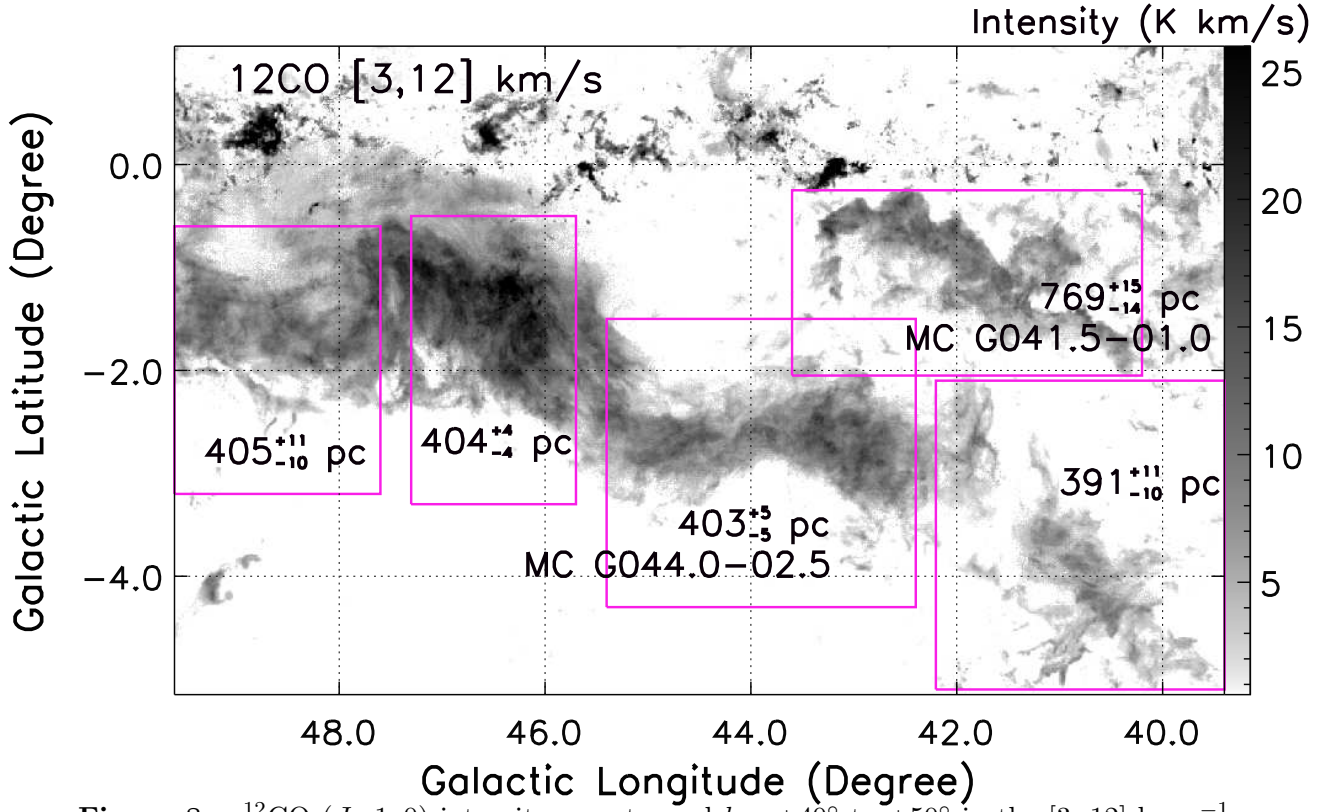


Figure 8. ^{12}CO ($J=1-0$) intensity map toward $l \sim +40^\circ$ to $+50^\circ$ in the $[3, 12]$ km s^{-1} interval. The distances of the corresponding molecular gas are labeled on the map. Note that distances in the map are estimated for the areas indicated by the rectangles but only using regions with high-integrated CO intensity (see the threshold in the text).

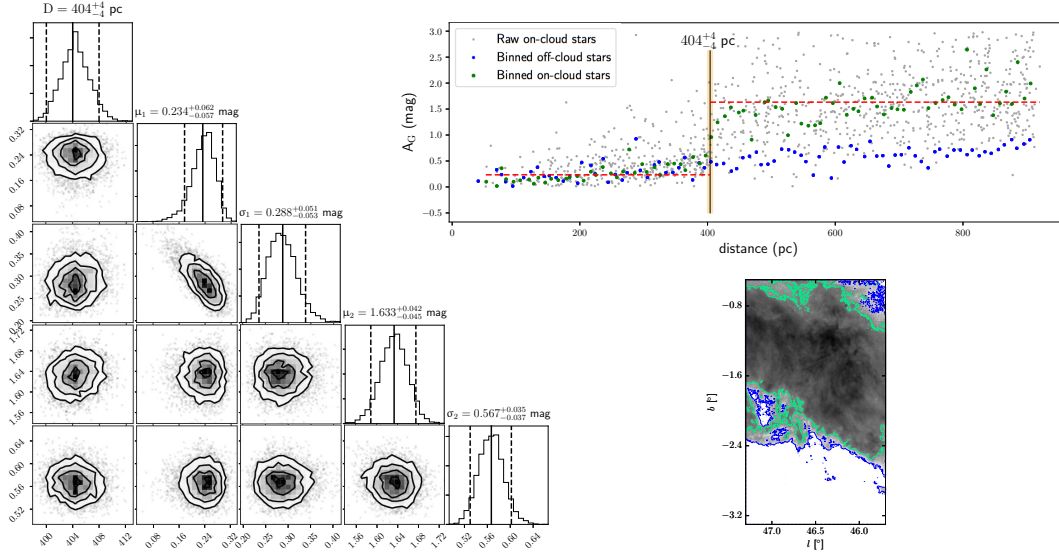


Figure 9. The estimated distance of a part of MC G044.0–02.5. The green and blue points are on- and off-cloud stars, respectively. The dashed red lines are the modeled extinction A_G . The vertical line indicates the jump in the distance– A_G space. The distance is estimated from the raw on-cloud Gaia DR2 (gray points). The shadow area in the upper right panel is the 95% HPD distance range. The relationships between the fitting parameters are shown in the left panel. The integrated CO emission is shown in the right corner plot. Please see the details in [Yan et al. \(2019\)](#).

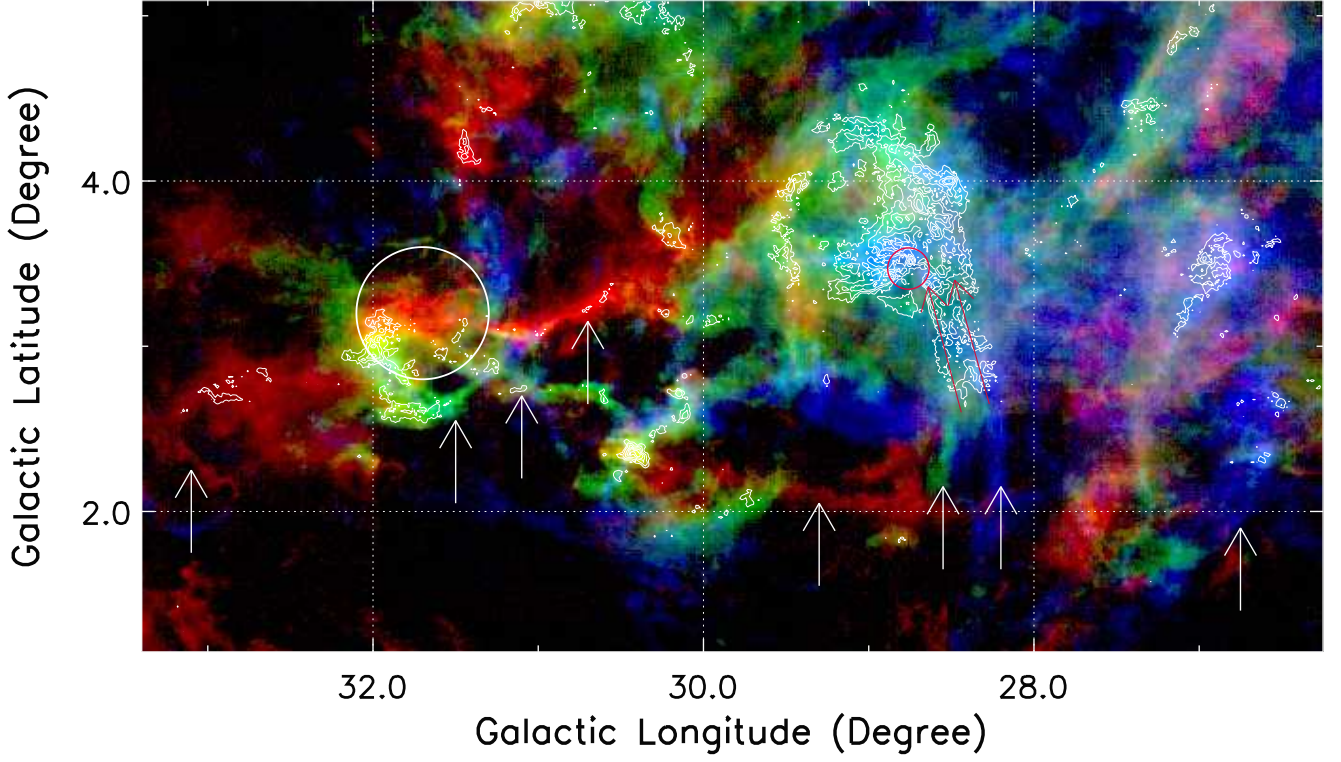


Figure 10. Integrated ^{13}CO ($J=1-0$) emission in the interval of $[4.5, 7.0]$ km s^{-1} (blue), $[7.0, 9.5]$ km s^{-1} (green), and $[9.5, 12.0]$ km s^{-1} (red) toward the H II region W40 (the red circle at $l = 28.8$ and $b = 3.5$ with a diameter of $0.2''$), overlaid with the C^{18}O ($J=1-0$) integrated emission contours of 0.5, 1.5, 2.5, 3.5, and 4.5 K km s^{-1} . The white circle at $l = 31.7$ and $b = 3.2$ with a diameter of $0.8''$ shows the region with higher ^{12}CO peak temperatures (see Figure 2). The star formation activities (e.g., the Serpens NE cluster and H II region W40) are responsible for the relatively high CO temperature in such regions. The white arrows show some typical filamentary structures seen in ^{13}CO emission. The red arrows indicate the direction of PV diagrams shown in Figure 11.

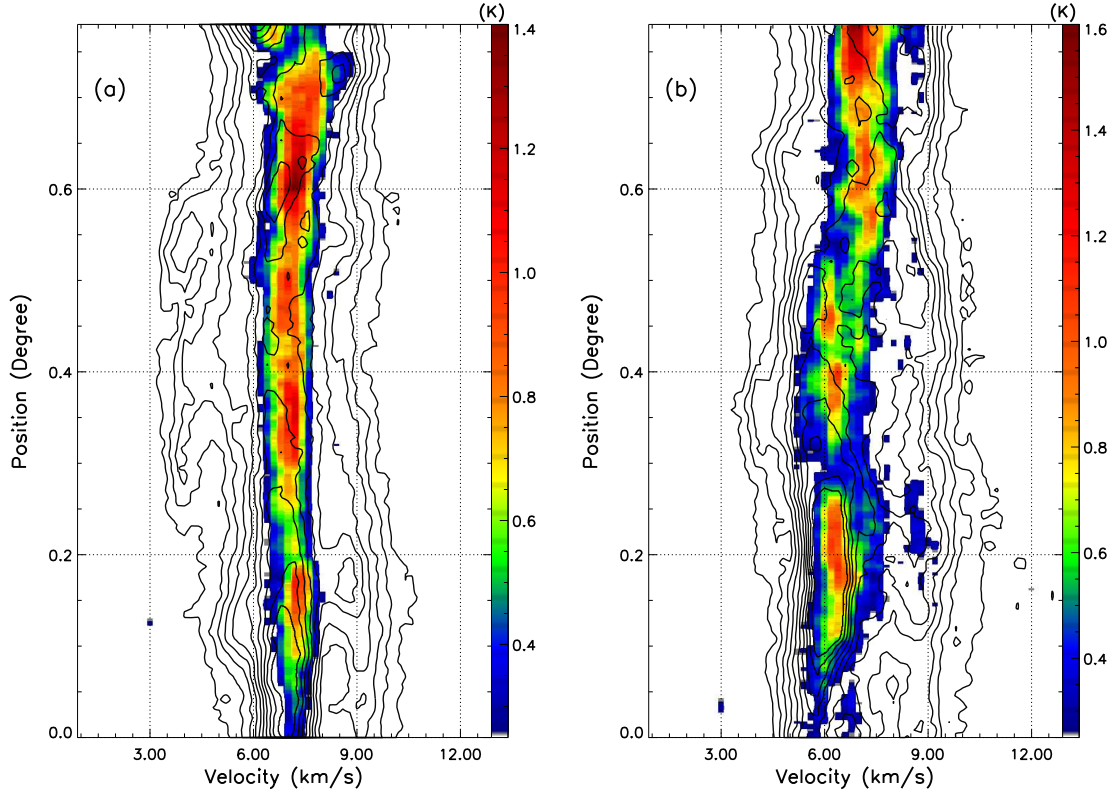


Figure 11. Position–velocity diagrams of the C^{18}O (color) and ^{13}CO (contours) emission of two filamentary structures labeled with red arrows in Figure 10, i.e., panel (a) from ($l = 28^\circ 44$, $b = 2^\circ 60$) to ($l = 28^\circ 64$, $b = 3^\circ 36$); and panel (b) from ($l = 28^\circ 27$, $b = 2^\circ 65$) to ($l = 28^\circ 48$, $b = 3^\circ 40$). The two slices have a length of $0^\circ 78$ and a width of $0^\circ 14$. The contours of the ^{13}CO emission start from 0.3 K with a step of 0.3 K.

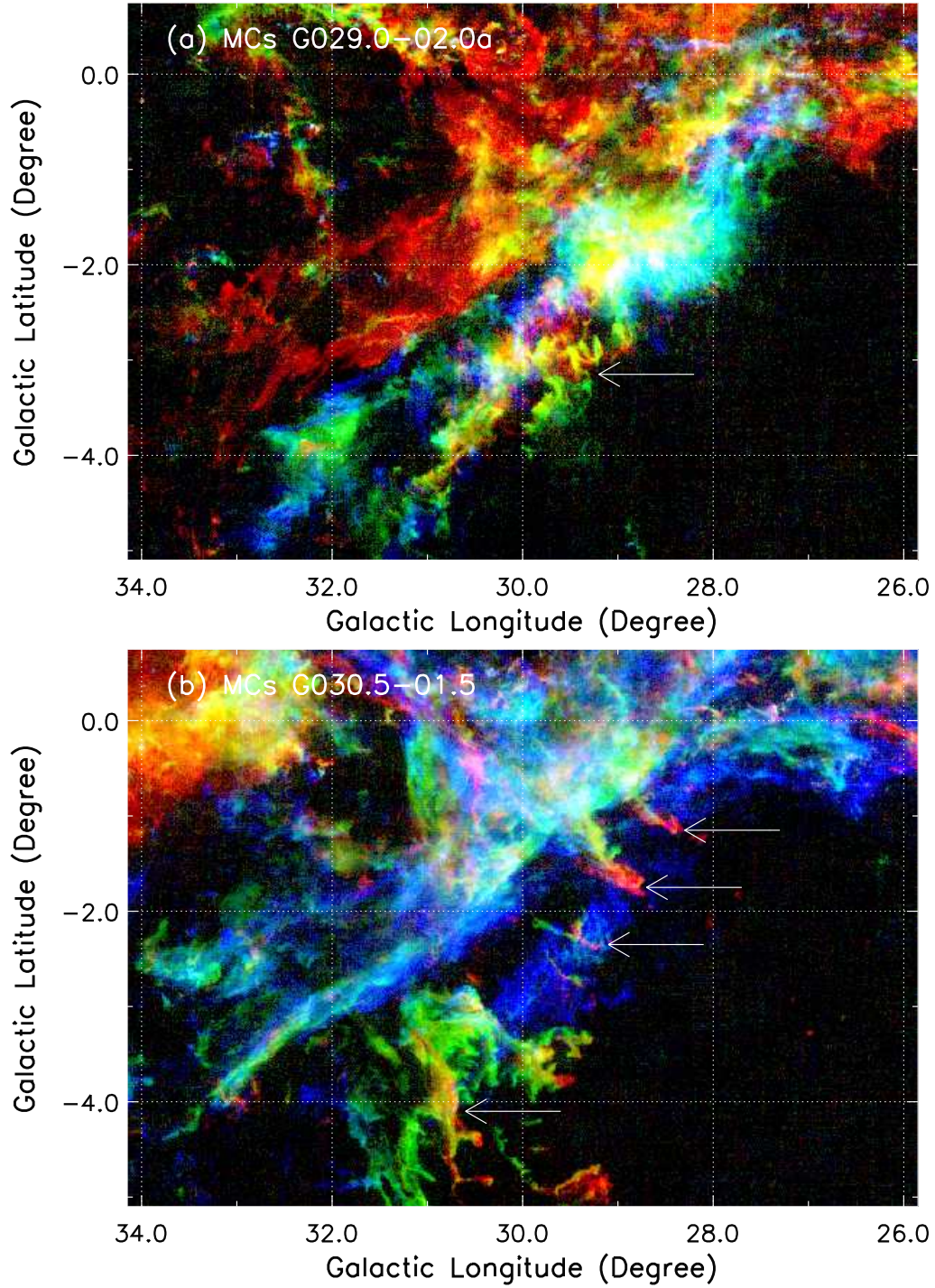


Figure 12. Panel (a): integrated ^{12}CO ($J=1-0$) emission in the interval of [1.0, 3.0] km s^{-1} (blue), [3.0, 5.0] km s^{-1} (green), and [5.0, 7.0] km s^{-1} (red) toward MCs G029.0-02.0a at a distance of ~ 260 pc. Panel (b): integrated ^{12}CO ($J=1-0$) emission in the interval of [6.0, 8.0] km s^{-1} (blue), [8.0, 10.0] km s^{-1} (green), and [10.0, 12.0] km s^{-1} (red) toward MCs G030.5-01.5 at the distance of ~ 400 pc. The white arrows indicate protruding structures perpendicular to the elongated molecular gas.

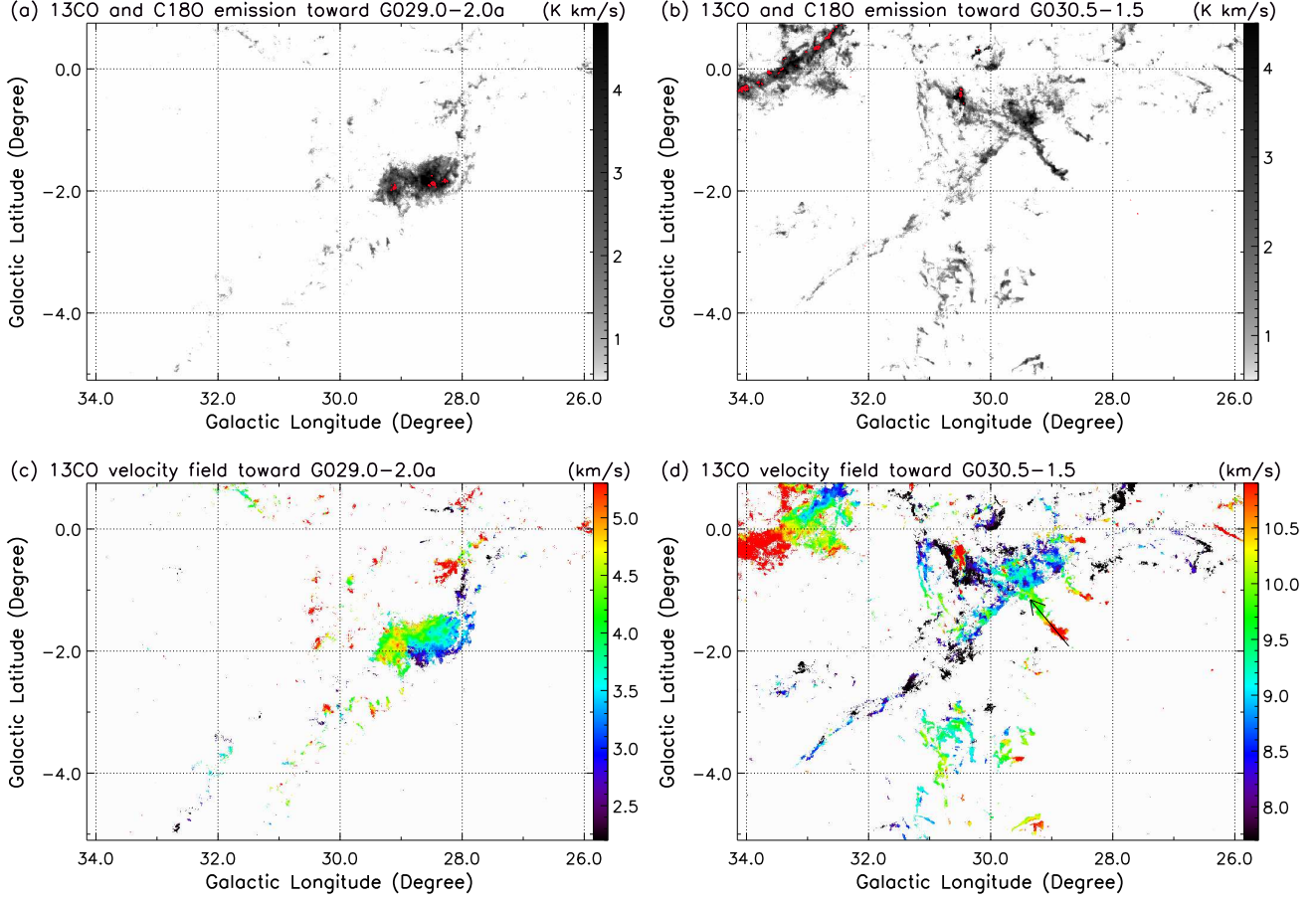


Figure 13. Panel (a): integrated ^{13}CO ($J=1-0$) emission (gray) and C^{18}O ($J=1-0$) emission (red contours, 0.4, 0.8, and 1.2 K km s^{-1}) toward MCs G029.0–02.0a in the velocity range of $[1.0, 7.0] \text{ km s}^{-1}$. Panel (b): same as panel (a) but for MCs G030.5–01.5 in the velocity range of $[6.0, 12.0] \text{ km s}^{-1}$. Panel (c): intensity-weighted ^{13}CO mean velocity (first moment) map of MCs G029.0–02.0a. Panel (d): same as panel (c) but for MCs G030.5–01.5. The black arrow indicates the direction of the PV diagram shown in Figure 14.

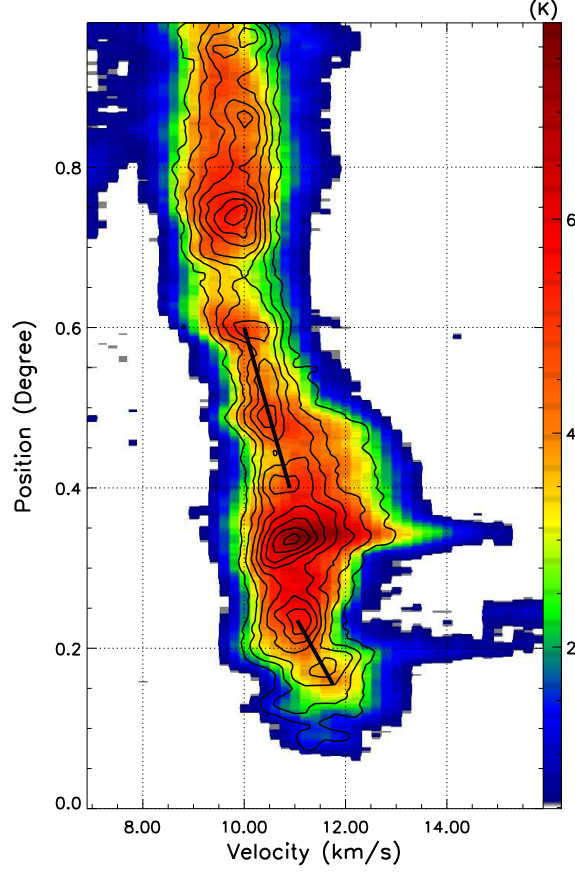


Figure 14. Position–velocity diagram of the ^{12}CO (color) and ^{13}CO (contours) emission of the protruding structure labeled with the black arrow in Figure 13, i.e., from $(l = 28^\circ.72, b = -1^\circ.92)$ to $(l = 29^\circ.35, b = -1^\circ.36)$. The slice has a length of $\sim 1^\circ$ and a width of $0^\circ.14$ from the ^{13}CO emission. The contours of ^{13}CO emission start from 0.3 K with a step of 0.3 K. The black lines indicate the velocity gradient of $\sim 0.7 - 1.3 \text{ km s}^{-1} \text{ pc}^{-1}$ for the CO gas at the distance of $\sim 400 \text{ pc}$.

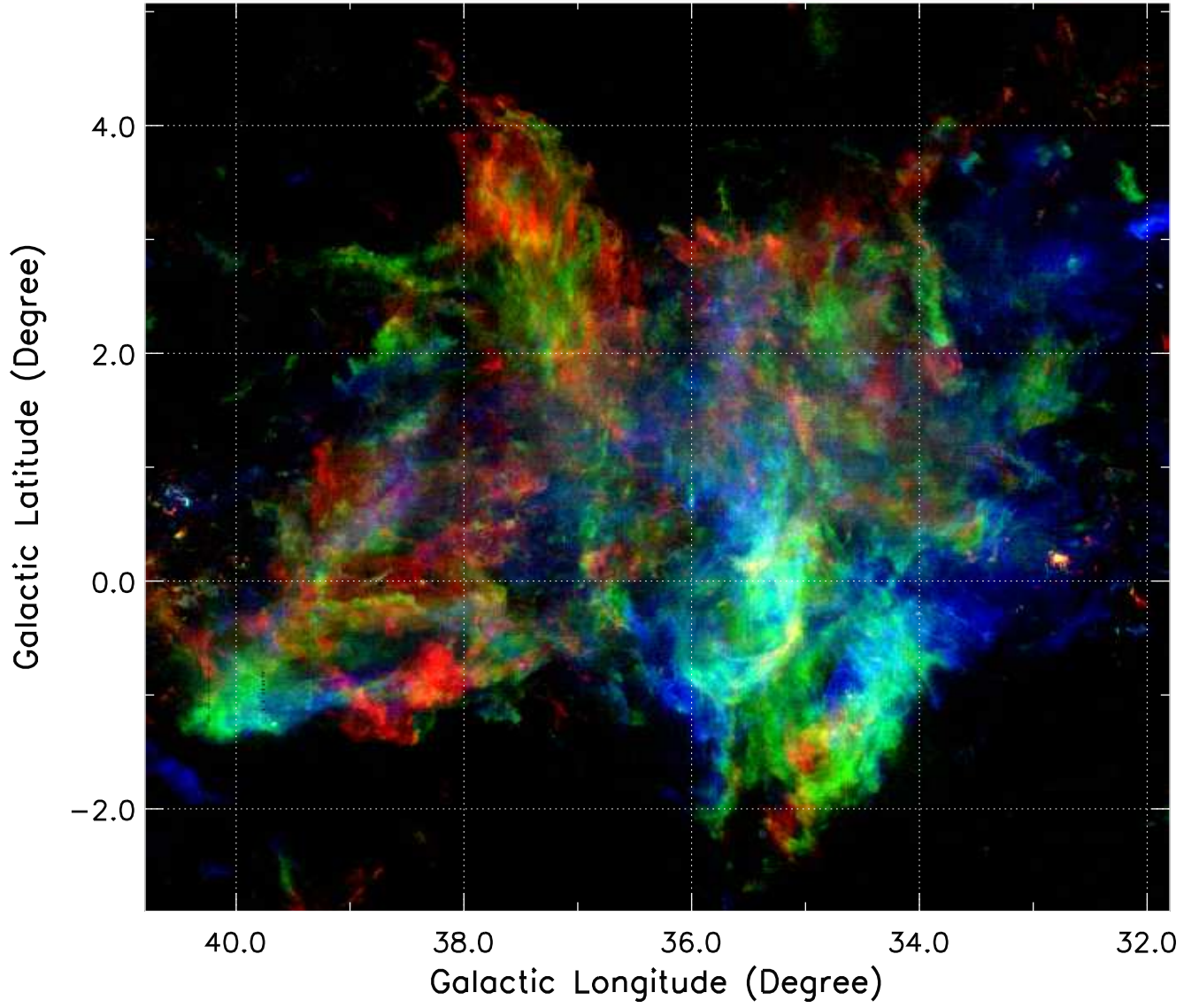


Figure 15. Integrated ^{12}CO ($J=1-0$) emission in the interval of $[11.0, 13.0]$ km s^{-1} (blue), $[13.0, 15.0]$ km s^{-1} (green), and $[15.0, 17.0]$ km s^{-1} (red) toward the GMC complex G036.0+01.0 at the distance of $\sim 560\text{--}670$ pc.

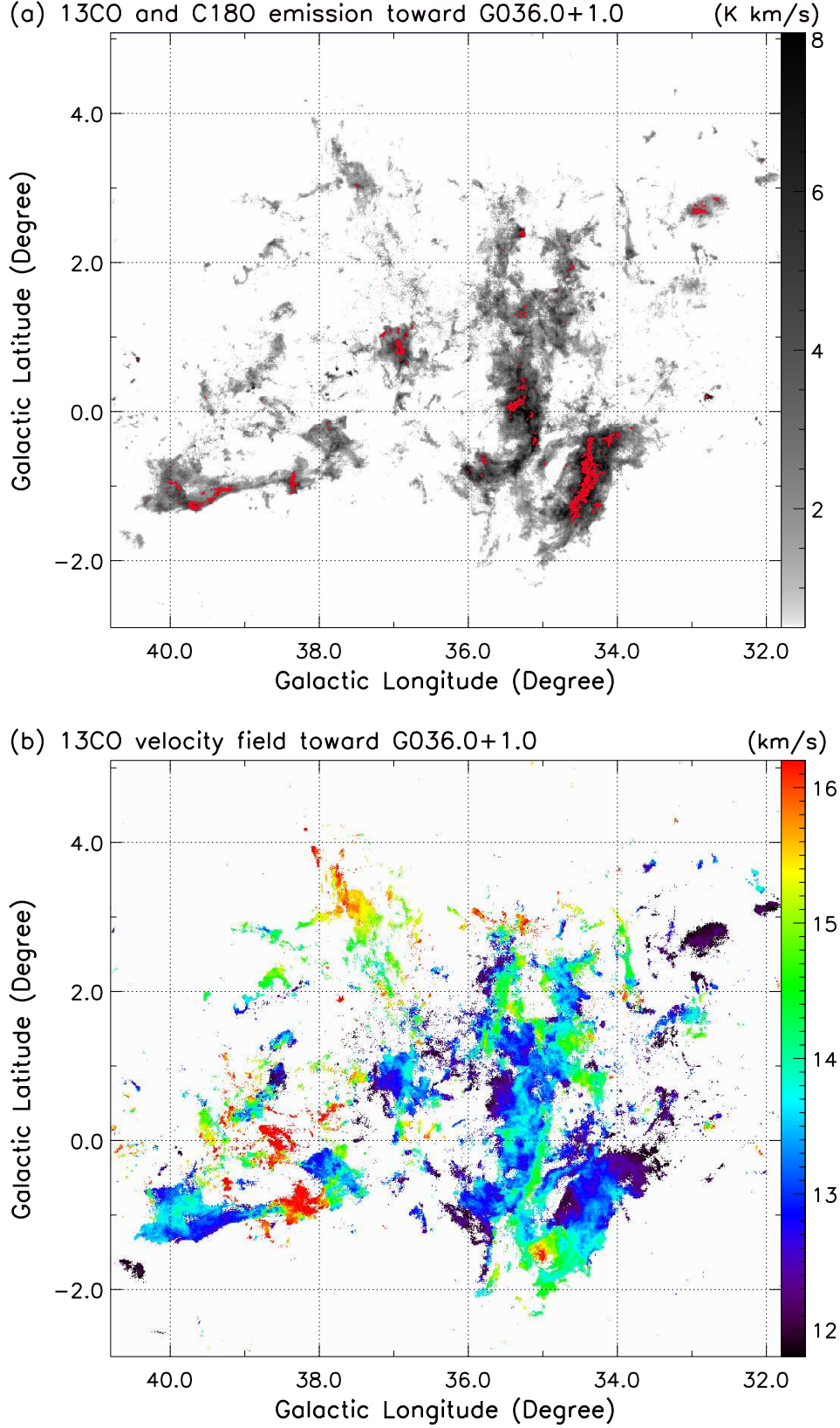


Figure 16. Panel (a): integrated ^{13}CO ($J=1-0$) emission (gray) and C^{18}O ($J=1-0$) emission (red contours, 0.4, 0.8, 1.2, 1.6, and 2.0 K km s $^{-1}$) toward the GMC complex G036.0+01.0 in the velocity interval of [11.5, 16.5] km s $^{-1}$. Panel (b): intensity-weighted ^{13}CO mean velocity (first moment) map of the GMC complex G036.0+01.0 in the same velocity range.

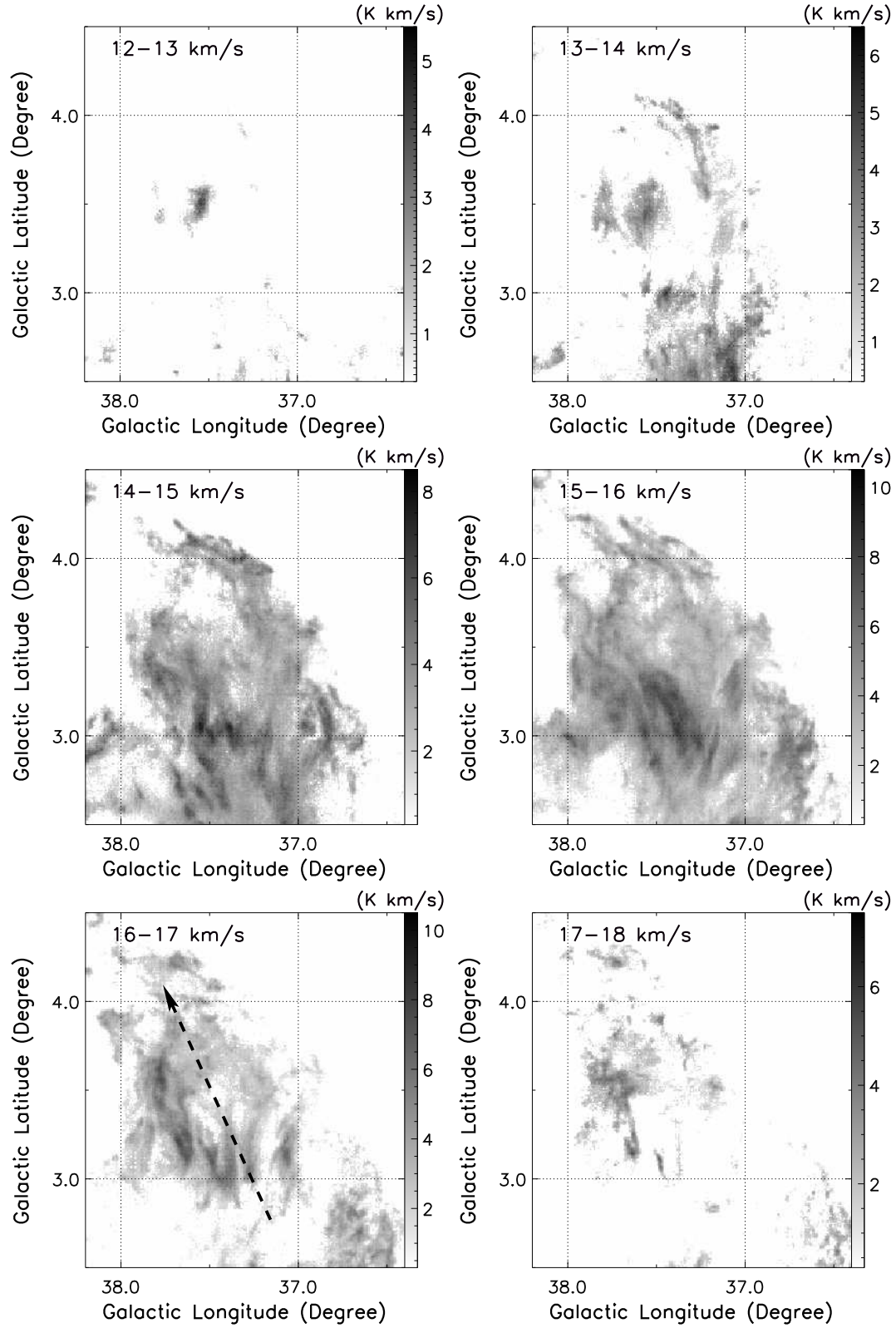


Figure 17. Channel maps of ^{12}CO emission toward the northeastern part of the GMC complex G036.0+01.0. The arrow indicates the direction of the large-scale elongated CO structure.

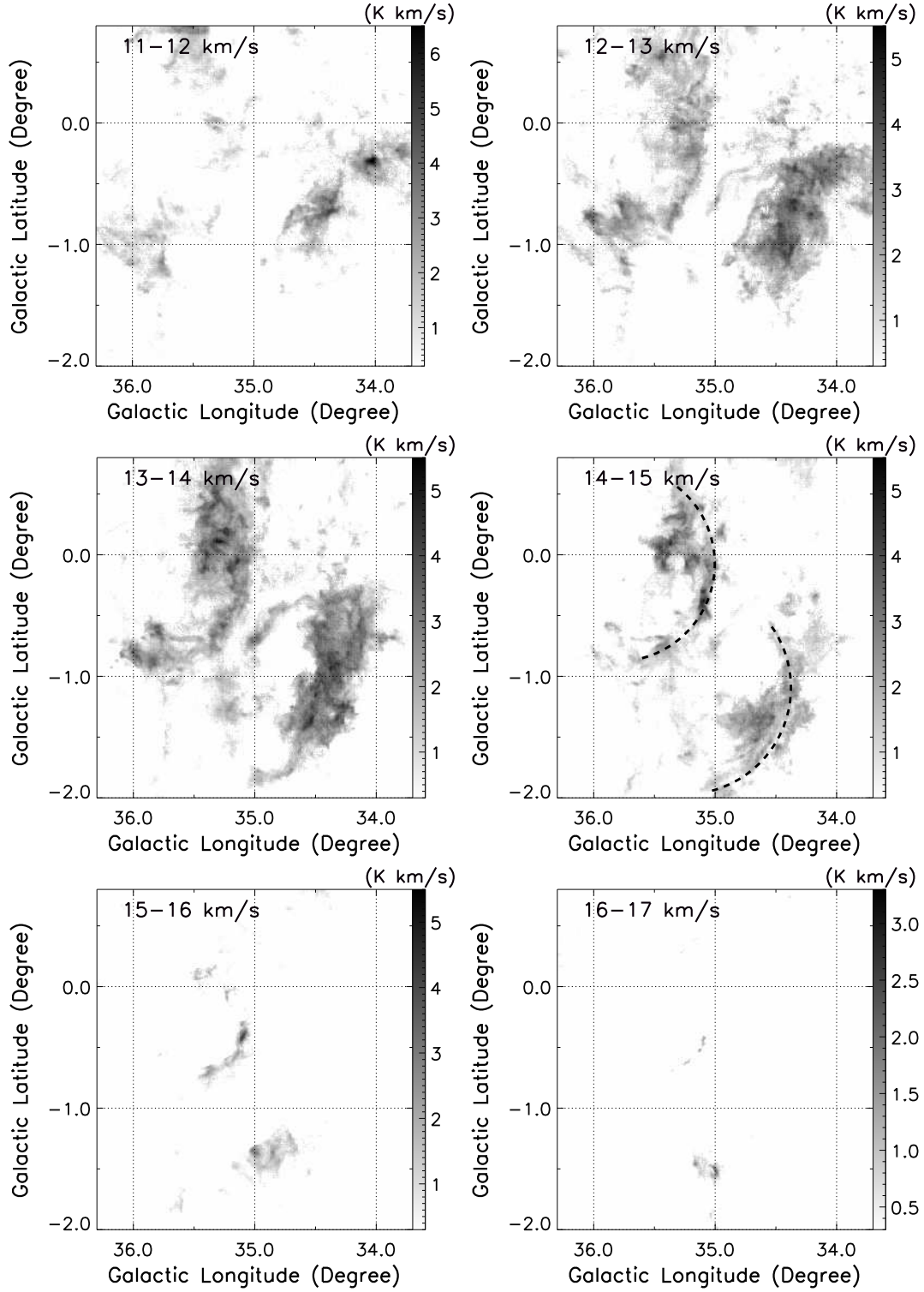


Figure 18. Channel maps of ^{13}CO emission toward the southwestern part of the GMC complex G036.0+01.0. The dashed lines indicate the large-scale arc-like structures traced by ^{13}CO emission.

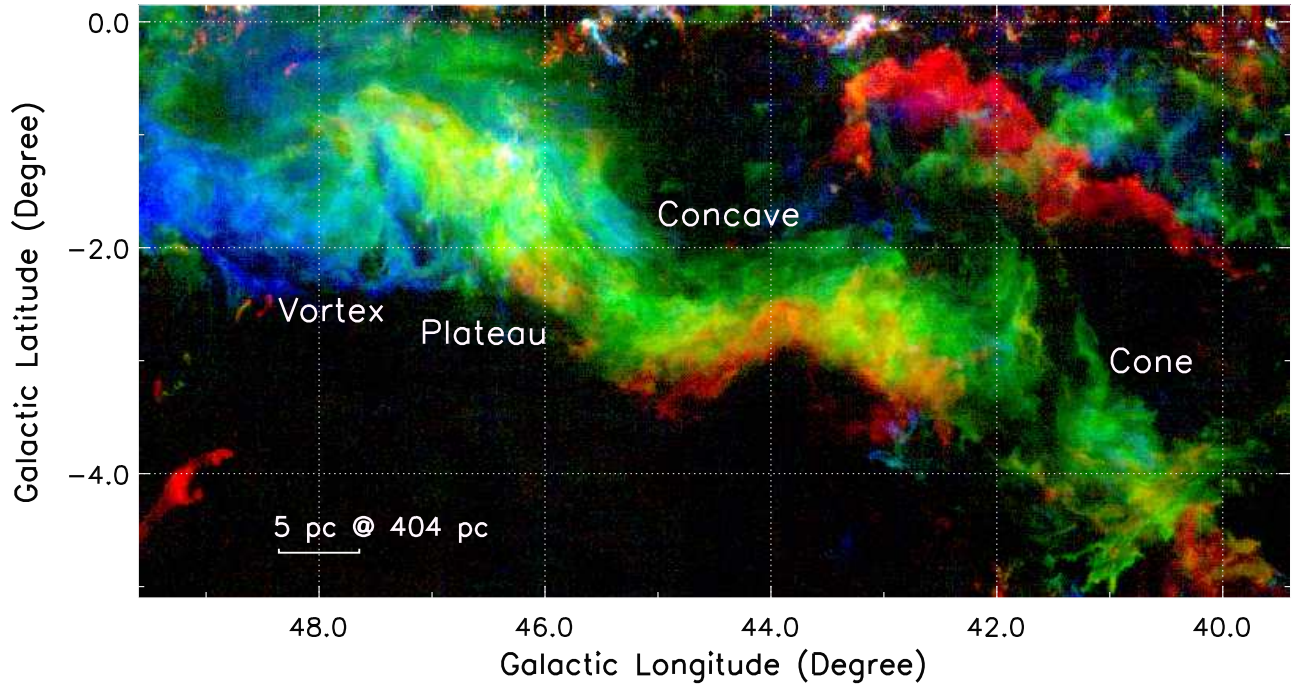


Figure 19. Integrated ^{12}CO ($J=1-0$) emission in the interval of [3.0, 6.0] km s $^{-1}$ (blue), [6.0, 9.0] km s $^{-1}$ (green), and [9.0, 12.0] km s $^{-1}$ (red) toward MC G044.0–02.5 at the distance of ~ 404 pc. The four sub-structures of the long filamentary MC are named as Vortex, Plateau, Concave, and Cone, respectively.

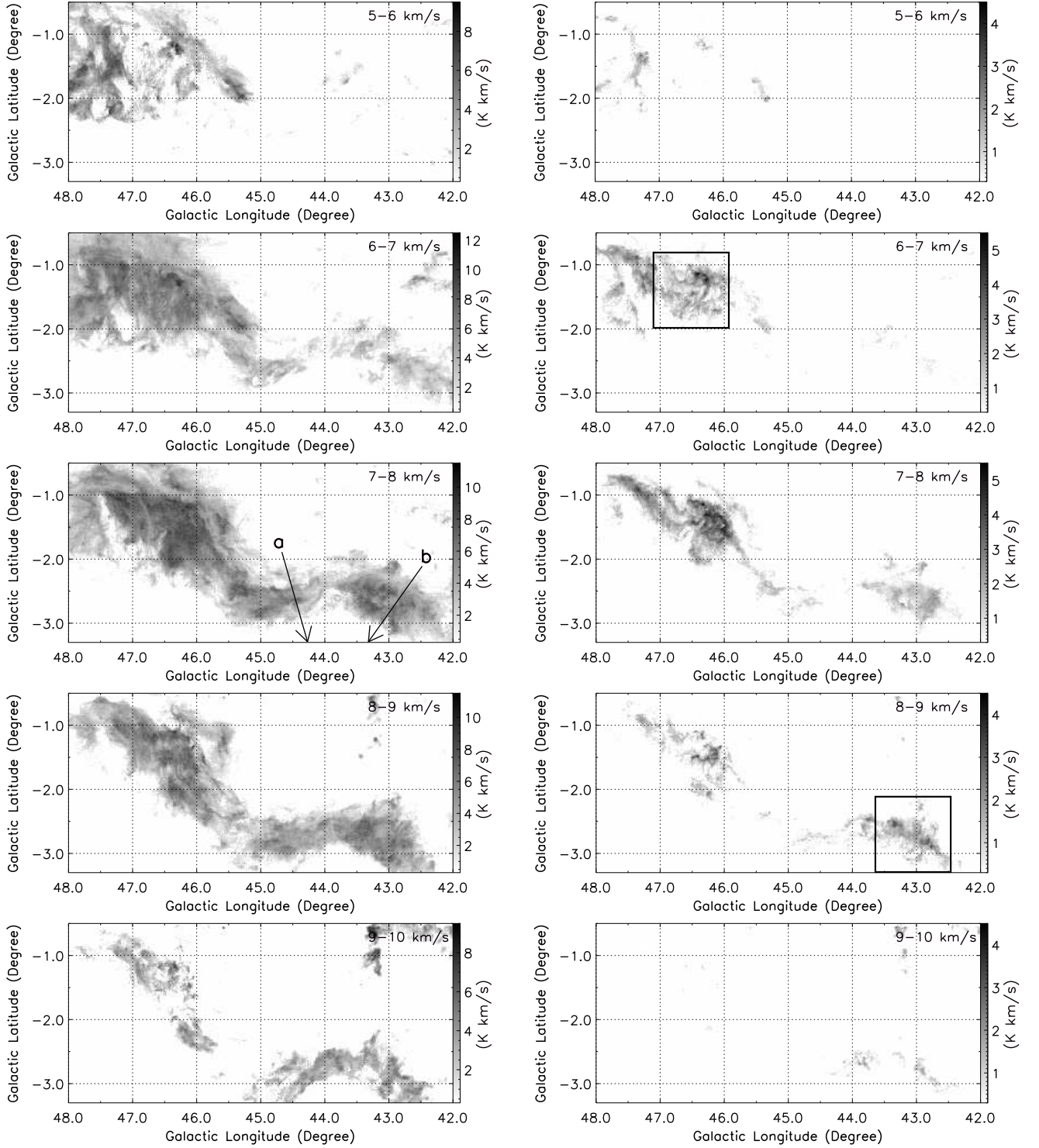


Figure 20. Channel maps of ^{12}CO emission (left panels) and ^{13}CO emission (right panels) toward the zoom-in region of the filamentary MC G044.0–02.5. The arrows show the direction of the velocity gradient (Figure 21) perpendicular to the long filamentary structure, while the two boxes display the typical regions of filamentary networks in the MC.

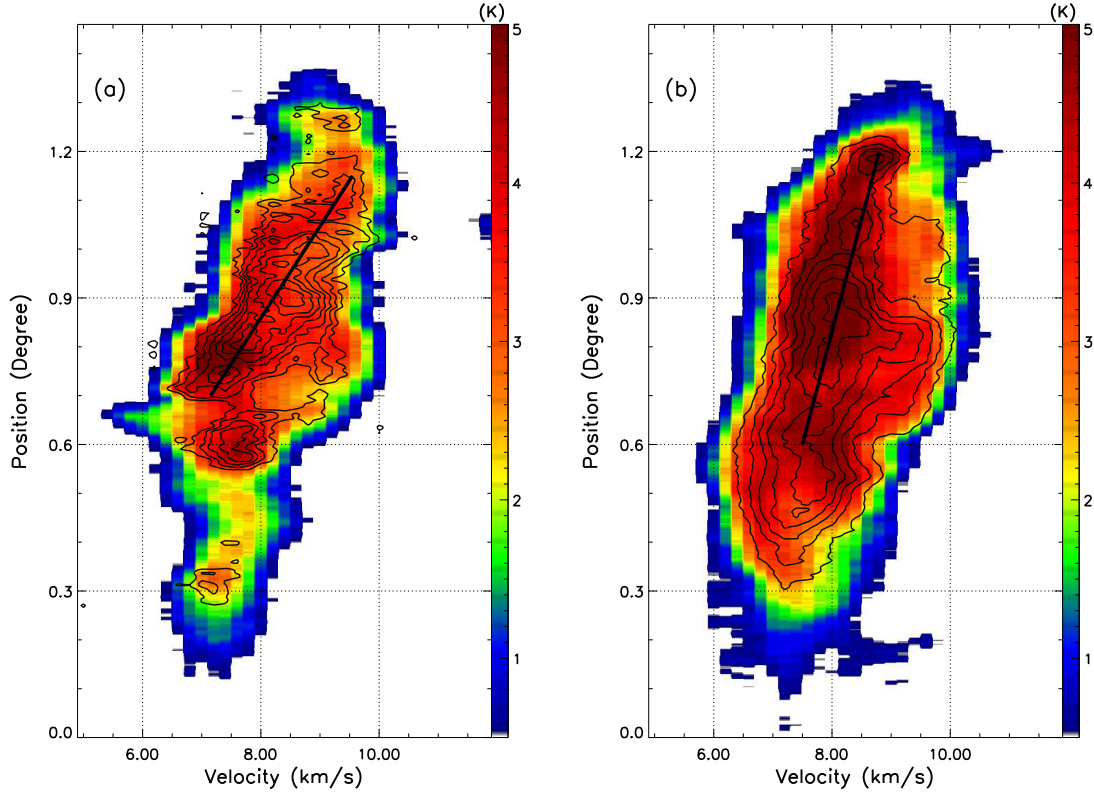


Figure 21. Position–velocity diagrams of the ^{12}CO (color) and ^{13}CO (contours) emission perpendicular to the long filamentary MC G044.0–02.5 (see arrows in Figure 20). The slice has a length of $1^{\circ}46'$ and a width of $0^{\circ}225'$. The contours of ^{13}CO emission start from 0.3 K with a step of 0.3 K. The black lines indicate the velocity gradient of $\sim 0.8 \text{ km s}^{-1} \text{ pc}^{-1}$ in panel (a) and $\sim 0.3 \text{ km s}^{-1} \text{ pc}^{-1}$ in panel (b) for the gas at a distance of $\sim 404 \text{ pc}$.

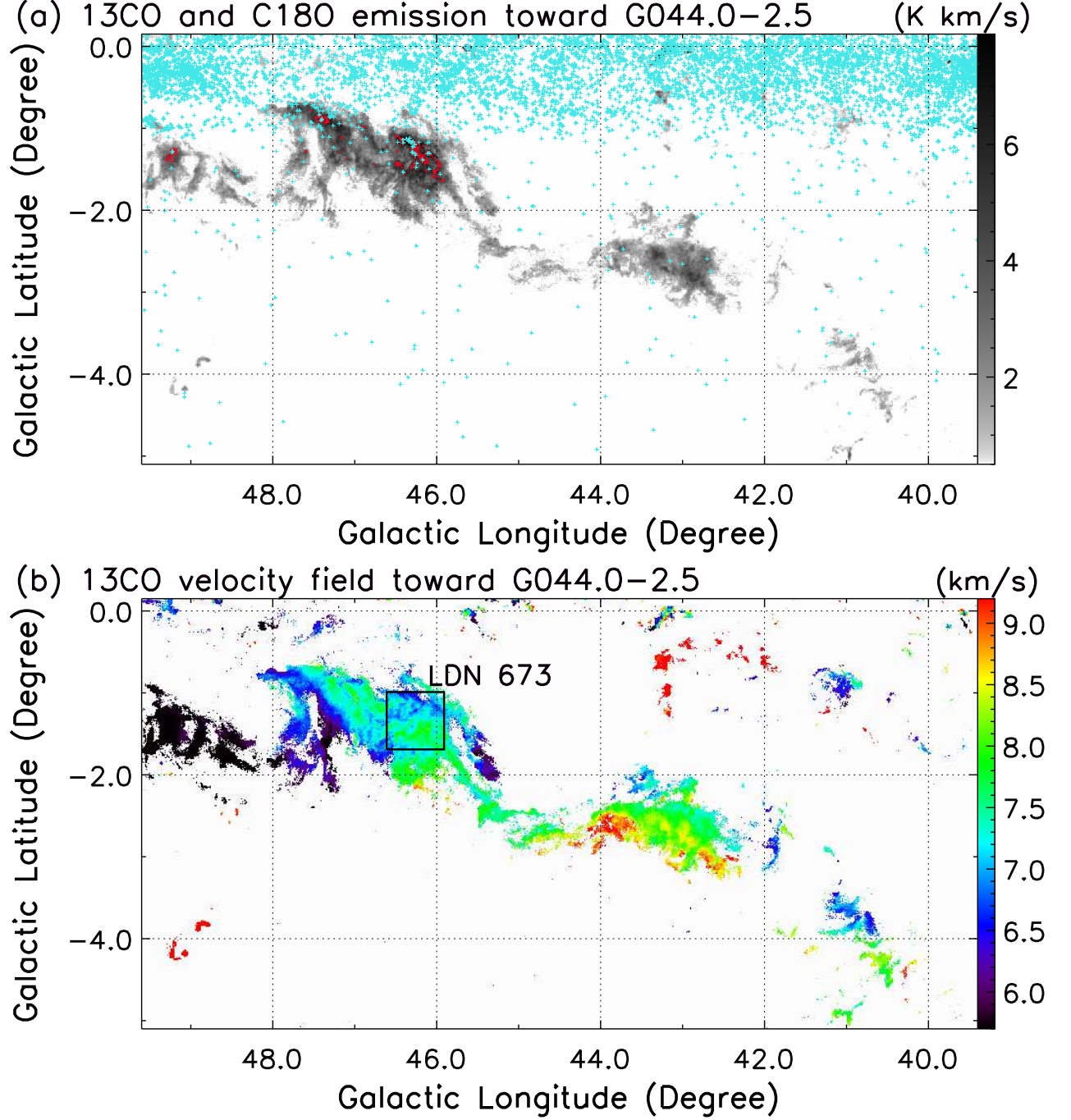


Figure 22. panel (a): integrated ^{13}CO ($J=1-0$) emission (gray) and C^{18}O ($J=1-0$) emission (red contours, 0.4, 0.8, 1.2, and 1.6 K km s $^{-1}$) toward MC G044.0-02.5 in the velocity interval of [3.0, 12.0] km s $^{-1}$. Cyan pluses indicate the YSO candidates (Class I and II sources and possible contamination of AGB stars) identified from the infrared multicolor criteria based on various IR data (see Table 1 and discussions in Zhang et al. 2019). The identified YSO candidates are found to be overdense in LDN 673, in which the enhanced C^{18}O emission is concentrated. Note that samples in the $|b| \lesssim 1^\circ$ region suffer high contamination due to the complex environment in the Galactic plane. Panel (b): intensity-weighted ^{13}CO mean velocity (first moment) map of MC G044.0-02.5 in the same velocity range. The black box shows the region of LDN 673.

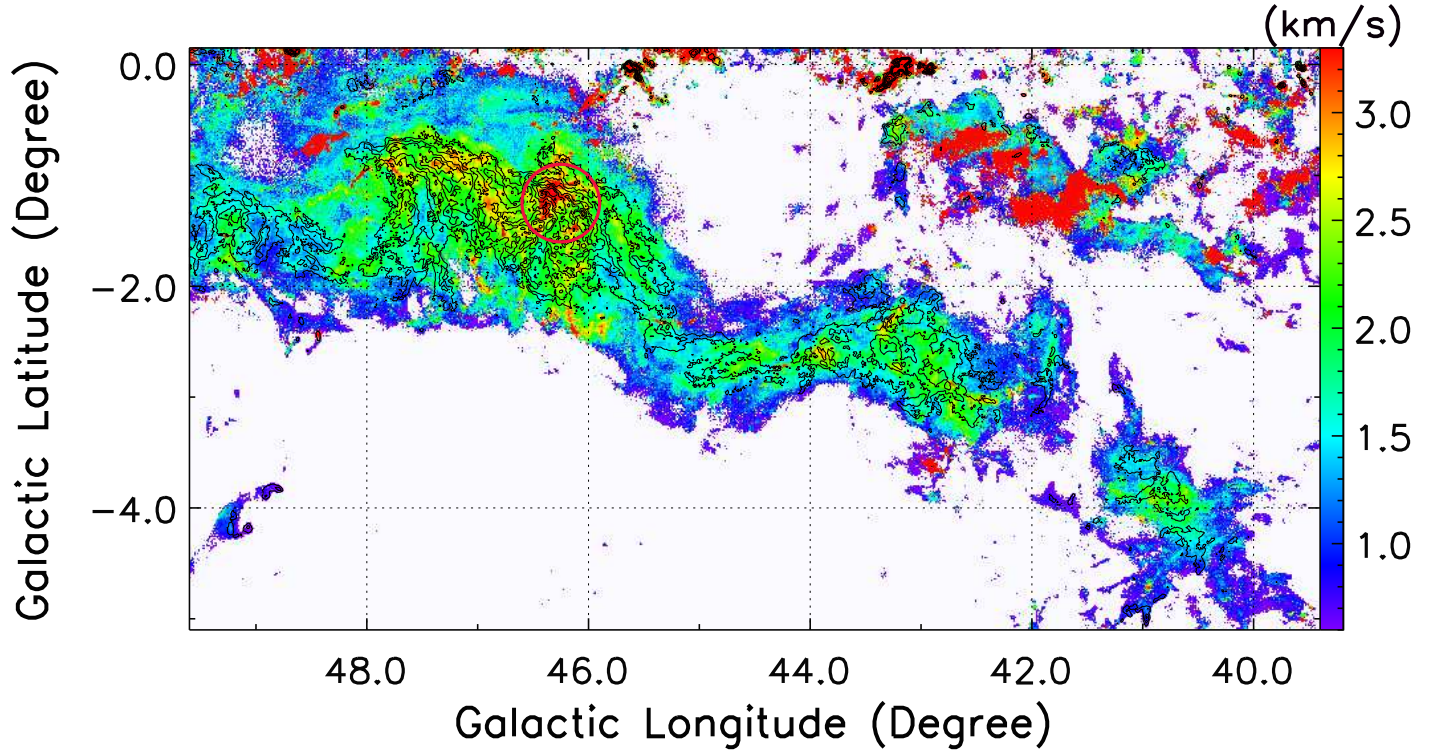


Figure 23. Intensity-weighted ^{12}CO line width (second moment) map of MC G044.0-02.5 in the $3.0\text{--}12.0 \text{ km s}^{-1}$ interval. The contours are 0.5, 2.0, 3.5, 5.0, 6.5, and 8.0 K km s^{-1} for ^{13}CO emission integrated in the same velocity range. The red circle indicates the hub-like region, i.e., LDN 673.

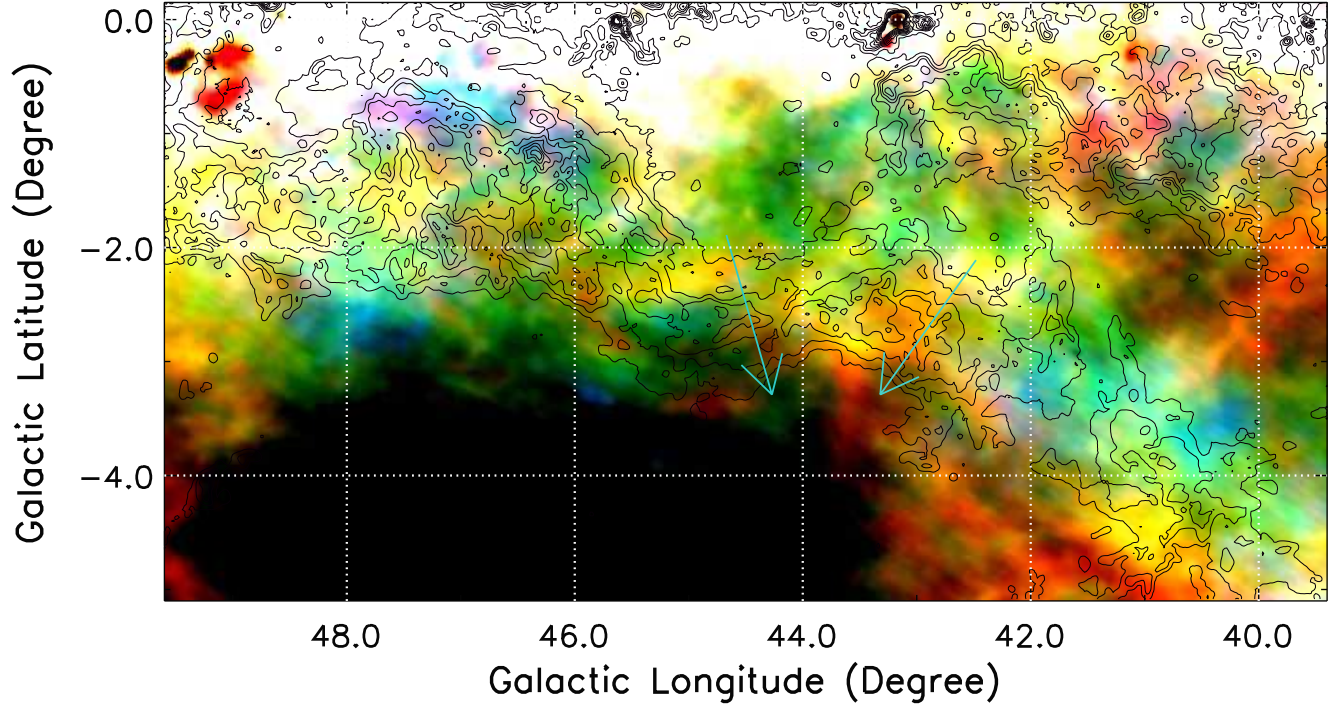


Figure 24. Integrated HI emission from Arecibo in the interval of $[4.0, 6.0]$ km s^{-1} (blue), $[6.0, 9.0]$ km s^{-1} (green), and $[9.0, 11.0]$ km s^{-1} (red) toward the MC G044.0–02.5. The contours, which are from 0.5 K km s^{-1} to 32.5 K km s^{-1} with a step of 4.0 K km s^{-1} , indicate the integrated ^{12}CO emission in the velocity range of $3.0\text{--}12.0 \text{ km s}^{-1}$. The cyan arrows are the same as those in Figure 20.

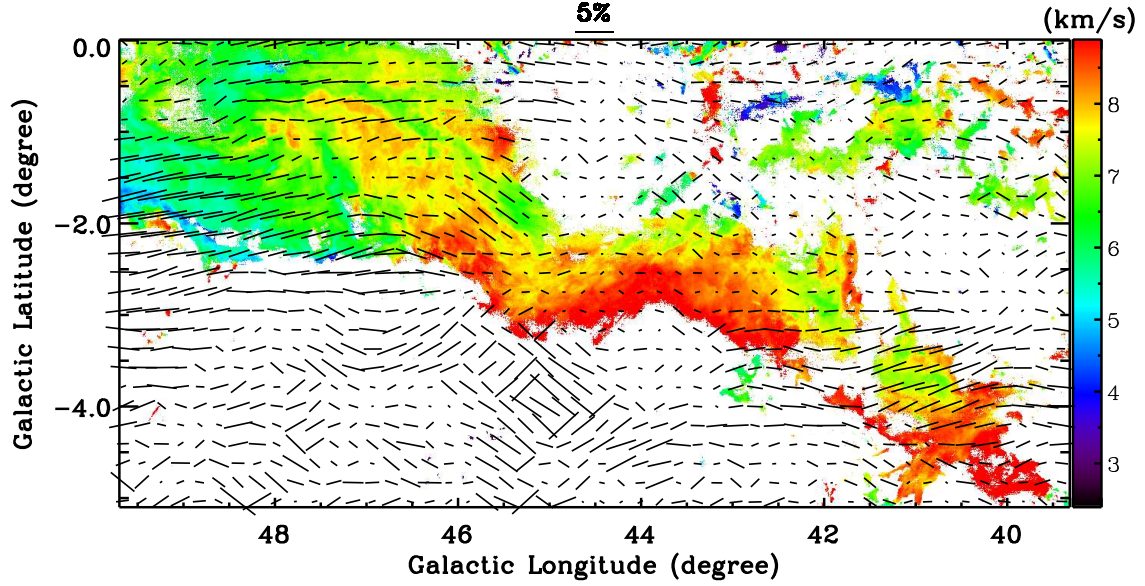


Figure 25. ^{12}CO velocity field of MC G044.0-02.5, overlaid with the orientations of the apparent magnetic field from the *Planck* 353 GHz data (Planck Collaboration et al. 2015). The 353 GHz data are smoothed to a resolution of $12''.5$ to improve the signal-to-noise ratio (S/N). The length of each polarization segment is proportional to the polarization fraction, and the position angle has been rotated by 90° . The uncertainties of polarization fraction and position angle are computed following the method described in Appendix B.1 of Planck Collaboration et al. (2015). Note that the polarization segments with $P/\sigma_P < 3$ are excluded in this plot.

Table 1. Parameters of Local Molecular Clouds toward the Aquila Rift

Name/Region	l range ($^{\circ}$)	b range ($^{\circ}$)	V_{LSR} (km s^{-1})	Area ^a (arcmin^2)	Distance ^b (pc)	Mass ^c (M_{\odot})	Note
(1)	(2)	(3)	(4)	(5)	(6)	(7)	(8)
W40a region	[25 $^{\circ}$ 8, 32 $^{\circ}$ 2]	[0 $^{\circ}$ 5, 5 $^{\circ}$ 1]	[0, 6]	1.4×10^4	235^{+4}_{-4}	2.2×10^3	$b \gtrsim 0^{\circ}$ in the left panel of Figure 5
W40b region	[25 $^{\circ}$ 8, 33 $^{\circ}$ 7]	[0 $^{\circ}$ 5, 5 $^{\circ}$ 1]	[4, 12]	1.0×10^5	474^{+6}_{-5}	1.4×10^5	Figure 10
MCs G029.0–02.0a	[27 $^{\circ}$ 2, 32 $^{\circ}$ 8]	[–5 $^{\circ}$ 1, –0 $^{\circ}$ 2]	[0, 7]	2.6×10^4	263^{+8}_{-8}	4.3×10^3	$b \lesssim 0^{\circ}$ in the left panel of Figure 5
MCs G029.0–02.0b	[26 $^{\circ}$ 3, 30 $^{\circ}$ 7]	[–5 $^{\circ}$ 1, –0 $^{\circ}$ 2]	[12, 25]	2.1×10^4	508–550	1.4×10^4 ^d	$b \lesssim 0^{\circ}$ in the right panel of Figure 5
MCs G030.5–01.5	[27 $^{\circ}$ 7, 33 $^{\circ}$ 8]	[–5 $^{\circ}$ 1, –0 $^{\circ}$ 1]	[4, 12]	3.5×10^4	403^{+15}_{-13}	1.3×10^4	$b \lesssim 0^{\circ}$ in the middle panel of Figure 5
GMC G036.0+01.0	[32 $^{\circ}$ 2, 40 $^{\circ}$ 4]	[–2 $^{\circ}$ 4, 5 $^{\circ}$ 1]	[8, 20]	1.3×10^5	555–673	2.0×10^5 ^e	Figures 7 and 15; the nickname of “Phoenix cloud”
MC G044.0–02.5	[39 $^{\circ}$ 3, 49 $^{\circ}$ 7]	[–5 $^{\circ}$ 1, 0 $^{\circ}$ 4]	[3, 12]	5.7×10^4	404^{+4}_{-4}	2.4×10^4	Figures 8 and 19; the nickname of “River cloud”
MC G041.5–01.0	[40 $^{\circ}$ 0, 43 $^{\circ}$ 4]	[–2 $^{\circ}$ 1, –0 $^{\circ}$ 2]	[9, 13]	7.0×10^3	769^{+15}_{-14}	9.1×10^3	the upper-right part in Figure 8

NOTE— ^a The area is defined by the integrated ^{12}CO emission in the corresponding velocity interval. ^b The distance is estimated based on the MWISP CO data and the Gaia DR2. The 5% systematic error is not included. ^c The total mass is estimated from the integrated ^{12}CO emission using the mean CO-to- H_2 mass conversion factor of $2 \times 10^{20} \text{ cm}^{-2} (\text{K km s}^{-1})^{-1}$ (see Section 3.3). ^d Adopting a mean distance of 530 pc for calculating the total mass of the MCs. ^e Adopting a mean distance of 610 pc for calculating the total mass of the GMC complex.